Håkon Laaveg Mjell

Sensorless Control of Synchronous Machines used in ASH

Master's thesis in Energy and Environmental Engineering
Supervisor: Roy Nilsen
June 2019

Master's thesis

NTNU
Norwegian University of Science and Technology
Faculty of Information Technology and Electrical Engineering
Department of Electric Power Engineering

NTNU
Kunnskap for en bedre verden

Håkon Laaveg Mjell

Sensorless Control of Synchronous Machines used in ASH

Master's thesis in Energy and Environmental Engineering
Supervisor: Roy Nilsen
June 2019

Norwegian University of Science and Technology
Faculty of Information Technology and Electrical Engineering
Department of Electric Power Engineering

NTNU
Norwegian University of
Science and Technology

Problem Description

For some high power applications, as for instance in Adjustable Speed Hydro (ASH), synchronous machines are used for power generation.

In this master thesis, sensorless control methods for such a Synchronous Generator with damper windings shall be developed. This means developing flux-models to be able to operate such machines without speed- and position- sensors. The performance of the control system depends on the accuracy of the parameters of the flux model. The main focus shall be:

- Sensorless control at low-speed operation
- Parameter sensitivity of the flux model

If time available, identification- and parameter estimation methods shall be investigated as well. In this master thesis, one should start to develop controller routines in our new control platform. Simulink with the Power System Library shall be used for implementation.

It will be a co-operation with the other Project-, Master- and PhD-students using the new control platform.

Abstract

Sensorless control of machines has become increasingly popular due to the reduced costs and increased reliability when avoiding a position sensor. The rotor position and speed can instead be estimated by the voltages and currents, using flux models. Sensorless control of a separately excited synchronous machine has been analyzed in this master thesis. A common disadvantage of sensorless control methods is the ability to estimate the rotor position at low speeds. In this thesis, existing flux models have been modified and improved in order to improve the performance in the low-speed region.

The main goal of this master thesis was to investigate sensorless operation at low speeds, and the parameter sensitivity of the flux model. The three-phase synchronous machine has been emulated by a Simulink model. A closed-loop observer combining the voltage model and the current model has been used, with a PI controller in the feedback loop. The PI controller was tuned by symmetrical optimum.

How estimation errors of the stator resistance, inductances in the d- and q-axis and damper winding resistances affected the sensorless performance was tested and analyzed. The simulations showed that the combination of the voltage and current model estimated the stator flux linkage accurately, except at low speeds. It was revealed that an erroneously estimated stator resistance and a voltage offset were the most critical sources of error. However, the errors could be reduced to some extent by using a PLL. The PLL was used to filter the rotor position input of the current controller, and was able to improve the performance when the stator resistance was underestimated. When a DC offset of 2V was applied to one of the stator voltages, the flux model performed better without the PLL at low speeds. At higher speeds, the PLL was able to reduce the errors slightly.

Sammendrag

Sensorløs kontroll av maskiner har blitt mer populært de seneste årene, siden man kan redusere kostnadene og øke påliteligheten ved å unngå posisjonssensor. Rotorens posisjon og hastighet kan istedenfor estimeres ved hjelp av strømmene og spenningene, ved å bruke fluksmodeller. Sensorløs styring av en separat magnetisert synkronmaskin har blitt analysert i denne masteroppgaven. En vanlig ulempe med sensorløs kontroll er den dårlige evnen til å estimere rotorposisjonen ved lave hastigheter. I denne oppgaven har eksisterende fluksmodeller blitt modifisert og forbedret slik at denne estimeringen kan bli mer nøyaktig ved lave hastigheter.

Hovedmålet med denne oppgaven var å undersøke sensorløs styring av motoren ved lave turtall, og parametersensitiviteten til fluksmodellen. En tre-fase synkronmaskin har blitt simulert ved hjelp av en Simulink-modell. En kombinasjon av spenningsmodellen og strømmodellen har blitt brukt til å estimere statorfluksforslyngningen, med en PI-regulator i tilbakesløyfen. Parametrene til PI-regulatoren har blitt dimensjonert med symmetrisk optimum.

Hvordan feilestimeringer av statorresistansen, induktansene i d- og q-aksene og motstanden i dempeviklingene påvirker estimeringen av statorfluksforslyngningen har blitt testet og analysert. Simuleringene viste at kombinasjonen av strøm- og spennings-modellen estimerte statorfluksforslyngningen med stor nøyaktighet, unntatt ved lave turtall. Det ble observert at feilestimering av statorresistansen og en offset i spenningsmålingene førte til de største feilene, selv om disse feilene kunne reduseres til en viss grad ved å bruke en PLL. PLL ble brukt til å filtrere rotorposisjonen som er input til strømmodellen, og det viste seg at ved å bruke PLL ble ytelsen kraftig forbedret når statorresistansen var underestimert. Når en spenningsoffset på 2V ble lagt til en av statorspenningene, fungerte modellen bedre uten PLL ved lave hastigheter. Ved høyere hastigheter derimot ble estimeringen av statorfluksforslyngningen noe mer nøyaktig ved bruk av PLL.

Preface

This master thesis is submitted to the Department of Electric Power Engineering at the Norwegian University of Science and Technology, and concludes my M. Sc. degree in Energy and Environmental Engineering. The master thesis has been written during the spring semester of 2019.

I would like to thank Professor Roy Nilsen, my supervisor, for his advice and guidance throughout both the specialization project and the master thesis. I would also like to thank the members of the PESC (Power Electronic Systems and Components) R&D software group for insightful discussions during weekly meetings.

Trondheim, June 2019
Håkon Laaveg Mjell

Table of Contents

List of Tables

List of Figures

Abbreviations

AC	=	Alternating Current
ASH	=	Adjustable Speed Hydro
DC	=	Direct Current
DFLC	=	Direct Flux Linkage Control
DMCC	=	DFLC Modulater based Current Control
DSP	=	Digital Signal Processing
DTC	=	Direct Torque Control
emf	=	electromotive force
FPGA	=	Field-Programmable Gate Array
ITC	=	Indirect Torque Control
mmf	=	magnetomotive force
PESC	=	Power Electronic Systems and Components
PI	=	Proportional Integral
PID	=	Proportional Integral Derivative
PLL	=	Phase Locked Loop
pu	=	per unit
PV	=	Photovoltaics
PWM	=	Pulse Width Modulation
R&D	=	Research & Development
VHDL	=	VHSIC Hardware Description Language
VHSIC	=	Very High Speed Integrated Circuits

List of Symbols

f	frequency
p	number of pole-pairs
n_s	synchronous speed
n	rotor speed
U	voltage
u	voltage
R	resistance
r	resistance
I	current
i	current
Ψ	flux linkage
ψ	flux linkage
L	inductance
ω_0	undamped resonance frequency
ω_n	nominal electric speed
x	reactance
x_{md}	magnetizing reactance in d-axis
x_{mq}	magnetizing reactance in q-axis
σ	leakage coefficient
ζ	damping ratio
T	time constant
T_e	electrical torque
τ_e	electrical torque
τ_{load}	load torque
ε	angle of stator flux linkage
θ	rotor position
φ	angle of stator current
δ	pole wheel angle
J	moment of inertia

Subscripts

s	stator
r	rotor
d	direct axis
q	quadrature axis
D	direct axis damper winding
Q	quadrature axis damper winding
f	field winding

Chapter 1: Introduction

1.1 Background

As a result of an increased focus on global warming and climate change, renewable energy sources like solar power and wind energy have become increasingly popular in the last decades [3]. The total global capacity of solar power increased from 3.7 GW in 2004 to 177 GW in 2014. During the same time period, the total capacity for wind power grew from 48 GW to 370 GW [3]. Both of these numbers are expected to grow further in the future [3, 18]. The drawback of these energy sources is the weather dependency. The weather changes throughout the year, so to be able to meet the energy demand at all times, an energy storage system can be used. The system allows for power to be stored when there is a power surplus, and release power when it is needed or economically beneficial. An environmentally friendly way of storing energy is through the use of hydropower plants [40]. This can be done by pumping water to the higher reservoir when there is a power surplus, storing it there for whenever it is demanded or profitable [6, 11]. In this way, the hydropower plant is able to balance the power supply that is becoming increasingly weather dependent and fluctuating.

Synchronous machines used for Adjustable Speed Hydro, or ASH, have been analyzed in this report. AC motors make up around 75 percent of variable speed drives [8]. The high efficiency and good overload capacity of electrically excited synchronous machines make them well suited for high-power applications [32, 33], as for instance pumped storage hydro. Good performance in the field weakening area is another strong point of synchronous machines [33]. Most electrically excited synchronous machines use a position sensor. However, sensorless drives

can be used for ship propulsion and large pump and blower drives [32]. Normally, synchronous machines rotate only at the synchronous speed, so to be able to pump with variable power, variable speed control must be applied [6]. According to [11], it is possible to increase the efficiency of the pumped storage hydro plant, both during generator and motor mode, by using adjustable speed control.

Sensorless control is a topic that has been widely discussed in the literature [9, 31, 32, 33, 38]. Sensorless control means controlling the machine without measuring rotor speed or position. Instead, the current and voltage can be measured, and these measurement values can be used to estimate the stator flux linkage. The stator flux linkage can then be used to estimate the rotor position and speed, that are needed for motor control. The advantages of sensorless control include increased reliability and decreased cost [35]. However, the cost aspect is less significant for large drives [33]. Operation at low speeds and crossing of zero speed is a well-known problem for many sensorless control methods. In recent years, research on sensorless control for low- and zero-speed applications has increased [27]. The performance of a synchronous machine while driving through zero-speed has been tested in this report through simulations in MATLAB/Simulink.

1.2 Relation to the specialization project

The topic of the specialization report [29] was sensorless control of synchronous machines, with a focus on drifting correction methods. The closed-loop observer combining the voltage model and the current model was tested in Simulink, and the use of P and PI controller in the feedback loop was compared and discussed. The initial plan was to continue the investigation of sensorless control of synchronous machines in the laboratory in this master thesis, but not enough time has been available. Consequently, this master thesis has been a continuation of the specialization project, and the tests have been carried out in Simulink. The same Simulink model has been used as a basis, but new simulations with a broader range of scenarios have been performed. The main focus has been tuning of the controllers in order to improve the Simulink model, and parameter sensitivity of the flux model, especially at low speeds.

Parts of Chapter 2 are based on the specialization project. This includes parts of Section 2.1 and Section 2.2. However, the theoretical parts of this master thesis are more detailed than they were in the specialization project. Furthermore, Chapter 3, 4 and 6 are strongly based on the specialization project. Section 1.1 is also very similar to the introduction in [29], as the background and motivation for the work remain the same.

1.3 Scope and limitations

All the tests of the synchronous machine have been performed in Simulink/MATLAB. Controller routines for a picoZed board have been developed in order to perform tests in the laboratory, but the full software structure and lab setup have not been ready in time for laboratory work to be done in this thesis. Field-weakening operation is one of the advantages of synchronous machines. However, no simulations have been performed in the field-weakening region.

1.4 Organization of the thesis

The first chapter explains the background and motivation for the thesis, as well as the scope and relation to the specialization project. Chapter 2 presents the fundamental theory about synchronous machines and includes the main equations used for the control. Sensorless control is discussed in Chapter 3, and Chapter 4 proposes different methods to mitigate the disadvantages of sensorless control. Chapter 5 describes the tuning of the controllers in the Simulink model. Chapter 6 shows and explains the simulation model used in this report, and Chapter 7 presents the results of the simulations performed in Simulink. Then, a discussion of the results is presented in Chapter 8. Finally, a conclusion is provided in the penultimate chapter, and suggestions for further work are presented in Chapter 10.

Chapter 2: Theory

In this chapter, the fundamental theory used for this master thesis will be presented. The first section provides general theory on synchronous machines. Moreover, Section 2.2 presents the main equations used for the modeling of the machine, including the physical equations, the Park and Clarke transformations and the transformed per unit equations. Different control methods for synchronous machines are presented and discussed in Section 2.3. The final section of this chapter provides basic theory on PID controllers. Parts of this chapter are retrieved from the specialization project of the author [29].

2.1 The synchronous machine

Synchronous machines are AC machines where the rotor speed under steady-state conditions is proportional to the frequency of the armature current [1, p. 245]. Equation 2.1 describes this relationship, where the synchronous speed is denoted by n_s [12, 20, 25]:

$$f = \frac{p \cdot n_s}{60} \tag{2.1}$$

A constant torque is produced only when the rotor rotates in synchronism with the magnetic field created by the armature currents. An induction machine, on the other hand, develops torque at non-synchronous speed, enabling it to avoid the stability problem of the synchronous machines. Today, more than 85% of industrial motors are induction motors [25]. However, synchronous machines are widely used for high-power applications [32]. Synchronous machines are

used whenever constant-speed operation is wanted, and synchronous machines also have the ability to control the power factor by varying the field current [25]. Another advantage of synchronous machines is the good performance in the field weakening area [33].

Synchronous machines are generally classified into two main types, the salient-pole type and the cylindrical-rotor type, depending on the rotor construction [25, p. 444]. The synchronous machines of the salient-pole type have a rotor where the poles project out from the core, leading to a non-uniform air-gap and a mmf that varies with the rotor position. The cylindrical-rotor machine (sometimes referred to as round-rotor [26]) on the other hand, has a rotor of a cylindrical form, providing a uniform air-gap and a mmf that is independent of the rotor position angle. Cylindrical-rotor machines are easier to model and are primarily used for high-speed turbo generators [26].

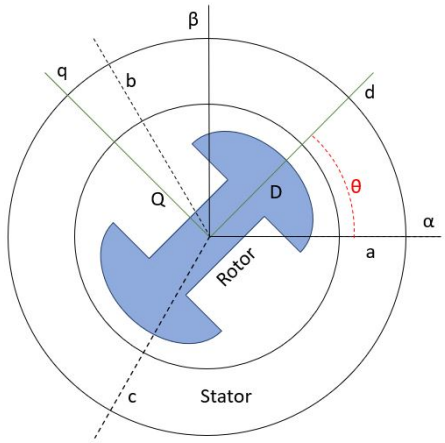

Figure 2.1: Model of the synchronous machine

A three-phase, salient-pole, four-pole synchronous machine has been analyzed in this master thesis. The stator windings are supplied by three-phase voltages that are symmetrically displaced by 120°. The Clarke [16] and Park [36] transformations can be applied to transfer these voltages into an equivalent two-phase system.

These transformations will be explained in detail in Section 2.2.2. The field winding is separately excited through slip rings.

Figure 2.1 illustrates a model of the synchronous machine and the different coordinate systems. The illustration shows a two-poled rotor rather than a four-poled for simplicity. The $\alpha\beta$-system is stationary, with the α-axis aligned with phase a, and β oriented 90° ahead. The dq-axes are attached to the rotor. The direct axis is aligned with the field winding, and the quadrature axis is aligned 90° ahead. θ is the angle between the stationary α axis and the rotating d-axis. The damper windings in the direct and quadrature direction, D and Q, are short-circuited.

2.2 Equations

The equations used for modeling of the synchronous machine are presented in this section. Lower-case letters are used for per unit quantities, while capital letters are used for the physical quantities. The same notation as in [35] has been used. The equation section has been separated into physical equations, transformed equations and per unit equations. The Clarke and Park transformations are explained in Section 2.2.2, before the transformed equations are presented. The final part of this section presents the alternative per unit equations that were implemented into the Simulink model in [11].

2.2.1 Physical model

The rotor and stator voltages of the synchronous machine can be described by Equation 2.2. The same matrix notation as in [35] is used.

$$\underline{\mathrm{U}}^{SR} = \mathbf{R}^{SR}\underline{\mathrm{I}}^{SR} + \frac{\mathrm{d}\underline{\Psi}^{SR}}{\mathrm{dt}} \tag{2.2}$$

The first term on the right side of the equation mark, $\mathbf{R}^{SR}\underline{\mathrm{I}}^{SR}$, represents the voltage drop in the winding, while the second term, $\frac{\mathrm{d}\underline{\Psi}^{SR}}{\mathrm{dt}}$, represents the induced back emf [10]. The stator voltages consist of phase a, b and c, and the rotor voltages consist of the field winding and the D and Q damper windings. As the

damper windings are short-circuited, $U_D = U_Q = 0$. Thus, the six following voltage equations, Equation 2.3-2.8, can be obtained [34].

$$U_{sa} = R_s I_{sa} + \frac{d\Psi_{sa}}{dt} \quad (2.3) \qquad U_f = R_f I_f + \frac{d\Psi_f}{dt} \quad (2.6)$$

$$U_{sb} = R_s I_{sb} + \frac{d\Psi_{sb}}{dt} \quad (2.4) \qquad U_D = R_D I_D + \frac{d\Psi_D}{dt} \quad (2.7)$$

$$U_{sc} = R_s I_{sc} + \frac{d\Psi_{sc}}{dt} \quad (2.5) \qquad U_Q = R_Q I_Q + \frac{d\Psi_Q}{dt} \quad (2.8)$$

To find a relationship between the flux linkage and the currents, the inductances of the synchronous machine need to be found. The following inductance equations are based on the work in [34] and [35]. First, the self-inductances of the stator windings can be written as:

$$L_a(\theta) = L_{a0} + L_{a\sigma} + L_g cos(2\theta) \quad (2.9)$$

$$L_b(\theta) = L_{a0} + L_{a\sigma} + L_g cos(2\theta - 240^\circ) = L_a(\theta - 120^\circ) \quad (2.10)$$

$$L_c(\theta) = L_{a0} + L_{a\sigma} + L_g cos(2\theta + 120^\circ) = L_a(\theta - 240^\circ) \quad (2.11)$$

It can be shown that the mutual inductances between the stator windings are given by:

$$L_{ab}(\theta) = L_{ba}(\theta) = -\frac{L_{a0}}{2} + L_g cos(2\theta - 120^\circ) \quad (2.12)$$

$$L_{bc}(\theta) = L_{cb}(\theta) = -\frac{L_{a0}}{2} + L_g cos(2\theta) \quad (2.13)$$

$$L_{ac}(\theta) = L_{ca}(\theta) = -\frac{L_{a0}}{2} + L_g cos(2\theta - 240^\circ) \quad (2.14)$$

The self-inductances on the rotor and the mutual inductances between the rotor windings are presented in Equation 2.15-2.20.

$$L_f = L_{f0} + L_{f\sigma} \quad (2.15) \qquad L_{fD} = L_{Df} \quad (2.18)$$

$$L_D = L_{D0} + L_{D\sigma} \quad (2.16) \qquad L_{DQ} = L_{QD} = 0 \quad (2.19)$$

$$L_Q = L_{Q0} + L_{Q\sigma} \quad (2.17) \qquad L_{fQ} = L_{Qf} = 0 \quad (2.20)$$

Both the self-inductances and the mutual inductances of the rotor windings in Equation 2.15-2.20 are independent of the rotor position. To get the full inductance matrix, the mutual inductances between the stator and rotor windings are also needed. The mutual inductances between phase a and the rotor windings are given by:

$$L_{af}(\theta) = L_{fa}(\theta) = L_{af}cos\theta \quad (2.21)$$

$$L_{aD}(\theta) = L_{Da}(\theta) = L_{aD}cos\theta \quad (2.22)$$

$$L_{aQ}(\theta) = L_{Qa}(\theta) = L_{aQ}cos(\theta + 90^\circ) = -L_{aQ}sin\theta \quad (2.23)$$

For phase b and c, the equations become similar but phase-shifted by 120° and 240°, respectively.

$$L_{bf}(\theta) = L_{fb}(\theta) = L_{af}cos(\theta - 120^\circ) \quad (2.24)$$

$$L_{bD}(\theta) = L_{Db}(\theta) = L_{aD}cos(\theta - 120^\circ) \quad (2.25)$$

$$L_{bQ}(\theta) = L_{Qb}(\theta) = -L_{aQ}sin(\theta - 120^\circ) \quad (2.26)$$

$$L_{cf}(\theta) = L_{fc}(\theta) = L_{af}cos(\theta - 240^\circ) \quad (2.27)$$

$$L_{cD}(\theta) = L_{Dc}(\theta) = L_{aD}cos(\theta - 240^\circ) \quad (2.28)$$

$$L_{cQ}(\theta) = L_{Qc}(\theta) = -L_{aQ}sin(\theta - 240^\circ) \quad (2.29)$$

The inductances in Equation 2.15-2.29 make up the entries of an inductance matrix, $\mathbf{L}^{SR}$, presented in Equation 2.30 [34].

$$\mathbf{L}^{SR} = \begin{bmatrix} L_a(\theta) & L_{ab}(\theta) & L_{ac}(\theta) & L_{af}(\theta) & L_{aD}(\theta) & L_{aQ}(\theta) \\ L_{ba}(\theta) & L_b(\theta) & L_{bc}(\theta) & L_{bf}(\theta) & L_{bD}(\theta) & L_{bQ}(\theta) \\ L_{ca}(\theta) & L_{cb}(\theta) & L_c(\theta) & L_{cf}(\theta) & L_{cD}(\theta) & L_{cQ}(\theta) \\ L_{fa}(\theta) & L_{fb}(\theta) & L_{fc}(\theta) & L_f & L_{fD} & 0 \\ L_{Da}(\theta) & L_{Db}(\theta) & L_{Dc}(\theta) & L_{Df} & L_D & 0 \\ L_{Qa}(\theta) & L_{Qb}(\theta) & L_{Qc}(\theta) & 0 & 0 & L_Q \end{bmatrix} \tag{2.30}$$

The machine used in this master thesis is of the salient-pole type. Thus both the self-inductance in the stator windings and the mutual inductance between the rotor and stator are depending on the rotor position θ. As the matrix in Equation 2.30 shows, all the inductances are dependent on the rotor position θ, except the damper windings and the field winding that are attached to the rotor. By applying the Park transformation, this dependency of the rotor position can be avoided. The Park transformation also makes vector control of the machine easier [11]. The Park transformation is explained in Section 2.2.2.

The flux linkage of the synchronous machine can then be described compactly by Equation 2.31, or in matrix notation through Equation 2.32.

$$\underline{\mathbf{\Psi}}^{SR} = \mathbf{L}^{SR}\underline{\mathbf{I}}^{SR}, \tag{2.31}$$

$$\begin{bmatrix} \Psi_a \\ \Psi_b \\ \Psi_c \\ \Psi_f \\ \Psi_D \\ \Psi_Q \end{bmatrix} = \begin{bmatrix} L_a(\theta) & L_{ab}(\theta) & L_{ac}(\theta) & L_{af}(\theta) & L_{aD}(\theta) & L_{aQ}(\theta) \\ L_{ba}(\theta) & L_b(\theta) & L_{bc}(\theta) & L_{bf}(\theta) & L_{bD}(\theta) & L_{bQ}(\theta) \\ L_{ca}(\theta) & L_{cb}(\theta) & L_c(\theta) & L_{cf}(\theta) & L_{cD}(\theta) & L_{cQ}(\theta) \\ L_{fa}(\theta) & L_{fb}(\theta) & L_{fc}(\theta) & L_f & L_{fD} & 0 \\ L_{Da}(\theta) & L_{Db}(\theta) & L_{Dc}(\theta) & L_{Df} & L_D & 0 \\ L_{Qa}(\theta) & L_{Qb}(\theta) & L_{Qc}(\theta) & 0 & 0 & L_Q \end{bmatrix} \begin{bmatrix} I_a \\ I_b \\ I_c \\ I_f \\ I_D \\ I_Q \end{bmatrix} \tag{2.32}$$

The upper index S in Equation 2.31 means that the physical stator windings are represented by stator fixed windings. The capital S means that it is a three-phase winding. Similarly, the upper index R means that the physical rotor windings are represented by windings that are fixed on the rotor. This is the same notation that is used in [34].

The torque balance gives the same equations as for a DC machine, given by [34, 35]:

$$J_{tot}\frac{d\Omega}{dt} = T_e - T_L \tag{2.33}$$

$$\frac{d\theta_{mech}}{dt} = \Omega \tag{2.34}$$

$$\omega = p \cdot \Omega \tag{2.35}$$

$$\theta = p \cdot \theta_{mech} \tag{2.36}$$

The electrical torque of a synchronous machine can be expressed by Equation 2.37 [34].

$$T_e = \frac{p}{2} \cdot (\underline{I}^{sr})^T \cdot \frac{\partial \mathbf{L}^{sr}}{\partial \theta} \cdot \underline{I}^{sr} \tag{2.37}$$

2.2.2 Clarke and Park transformation

To avoid the dependency of the rotor position, the Clarke and Park transformation can be used to transform the three-phase stator quantities to an equivalent two-phase system of direct- and quadrature-axis components. In this subsection, the Clarke and Park transformations will be explained.

The Clarke transformation, also called the alpha-beta (or $\alpha\beta\gamma$) transformation, transforms the three-phase quantities to a stationary two-phase system. The stator currents can be written as [16]:

$$i_a = i_\alpha + i_0 \tag{2.38}$$

$$i_b = -\frac{1}{2}i_\alpha + \frac{\sqrt{3}}{2}i_\beta + i_0 \tag{2.39}$$

$$i_c = -\frac{1}{2}i_\alpha - \frac{\sqrt{3}}{2}i_\beta + i_0 \tag{2.40}$$

where the zero-sequence current i_0 is defined as [16]:

$$i_0 = \frac{i_a + i_b + i_c}{3} \tag{2.41}$$

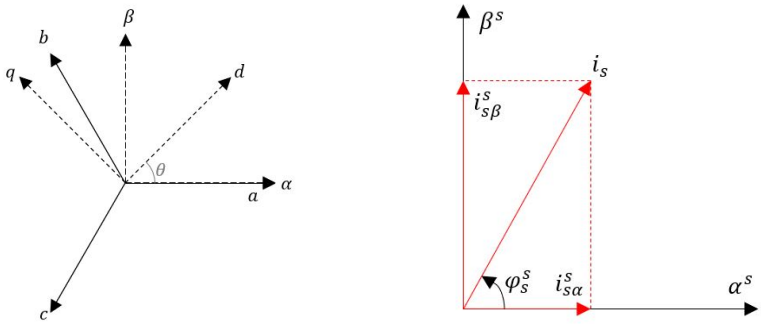

(a) Three-phase and two-phase quantities **(b)** i_s as the sum of α and β vectors

Figure 2.2: Illustrations of the three-phase and two-phase space vectors

Equation 2.38-2.40 can be derived using Figure 2.2. From Figure 2.2b it can be seen that the three-phase quantities can be represented as a sum of the α and β space vectors. Through the use of trigonometric functions and Figure 2.2a, the stator currents can be written as:

$$i_a = i_\alpha \tag{2.42}$$

$$i_b = -i_\alpha cos(60^\circ) + i_\beta cos(30^\circ) \tag{2.43}$$

$$= -\frac{1}{2} i_\alpha + \frac{\sqrt{3}}{2} i_\beta \tag{2.44}$$

$$i_c = -i_\alpha cos(60^\circ) - i_\beta cos(30^\circ) \tag{2.45}$$

$$= -\frac{1}{2} i_\alpha - \frac{\sqrt{3}}{2} i_\beta \tag{2.46}$$

The stator currents are used in Equation 2.38-2.40, but these equations also apply for the flux linkages and voltages, replacing i with ψ or v. The zero-sequence component can be omitted by assuming a balanced three-phase system, i.e. $i_a + i_b + i_c = 0$ [1]. Similarly, the two-phase currents can be found using the measurable three-phase current through Equation 2.47-2.48, assuming a balanced three-phase system [16, 35].

$$i_\alpha = i_a \tag{2.47}$$

$$i_\beta = \frac{\sqrt{3}}{2}(i_b - i_c) \tag{2.48}$$

After performing Clarke's transformation, Park's transformation can be used to turn the stationary two-phase system into a rotating one. As discussed in the previous section, the three stator phases in a salient-pole machine see a time-varying inductance. However, the transformed dq-quantities rotate with the rotor, as the direct axis is aligned with the axis of the field winding. Thus the transformed quantities see constant magnetic paths [1, p. 657]. This idea was first introduced by André Blondel, and the method is sometimes referred to as Blondel's two-reaction method. The concept was later refined and continued by R. E. Doherty, C. A. Nickle, and most notably R. H. Park in [36]. Before Park's transformation was formulated, only simplified models using second- or third-order differential equations could be used to describe AC machines [26]. Another motivating factor for the transformation is that a model with DC quantities at stationary conditions is wanted [35, p. 168].

Park's transformation transforms the stationary $\alpha\beta$-system to a rotating dq-reference frame, which is fixed to the rotor. The direct- and quadrature-currents can be described by Equation 2.49 and 2.50, respectively [36].

$$i_d = \frac{2}{3}(i_a cos\theta + i_b cos(\theta - 120^\circ) + i_c cos(\theta + 120^\circ) \tag{2.49}$$

$$i_q = -\frac{2}{3}(i_a sin\theta + i_b sin(\theta - 120^\circ) + i_c sin(\theta + 120^\circ) \tag{2.50}$$

This corresponds to multiplying the $\alpha\beta$-quantities with a transformation matrix T^r_{ss}, defined in Equation 2.51. It is also possible to go from the rotating to a stationary system by multiplying with the inverse transformation matrix, T^{-r}_{ss} [35].

$$\mathbf{T}^r_{ss} = \begin{bmatrix} cos\theta & sin\theta \\ -sin\theta & cos\theta \end{bmatrix} \tag{2.51}$$

$$\mathbf{T}^{-r}_{ss} = \begin{bmatrix} cos\theta & -sin\theta \\ sin\theta & cos\theta \end{bmatrix} \tag{2.52}$$

The relationship between the different frames can be expressed as [35]:

$$\underline{\mathrm{I}}^r_s = \mathbf{T}^r_{ss} \cdot \underline{\mathrm{I}}^s_s \tag{2.53}$$

$$\underline{\mathrm{I}}^s_s = \mathbf{T}^{-r}_{ss} \cdot \underline{\mathrm{I}}^r_s \tag{2.54}$$

$$\mathbf{T}^{-r}_{ss} = (\mathbf{T}^r_{ss})^{-1} \tag{2.55}$$

The full transformation matrix, T^r, that transforms between the physical three-phase quantities and the rotational dq-quantities, is given by Equation 2.56, while its inverse, T^{-r}, is defined in Equation 2.57. $\mathbf{I}$ is the identity matrix of dimension 2. This is because the rotor windings are unchanged, so both $\mathbf{T}^r_{rr}$ and its inverse $\mathbf{T}^r_{rr}$ become equal to $\mathbf{I}$.

$$\mathbf{T}^r = \begin{bmatrix} \mathbf{T}^r_{ss} & 0 \\ 0 & \mathbf{I} \end{bmatrix} \tag{2.56}$$

$$\mathbf{T}^{-r} = \begin{bmatrix} \mathbf{T}^{-r}_{ss} & 0 \\ 0 & \mathbf{I} \end{bmatrix} \tag{2.57}$$

2.2.3 dq equations

To find the transformed equations, the voltage, current and flux linkage equations from Section 2.2.1 can be multiplied with the transformation matrix T^r. The transformed voltage equations are presented in Equation 2.58-2.61.

$$U_{sd} = R_s I_{sd} + \frac{d\Psi_{sd}}{dt} - \omega\Psi_{sq} \quad (2.58) \qquad U_{rd} = R_{rd} I_{rd} + \frac{d\Psi_{rd}}{dt} \quad (2.60)$$

$$U_{sq} = R_s I_{sq} + \frac{d\Psi_{sq}}{dt} + \omega\Psi sd \quad (2.59) \qquad U_{rq} = R_{rq} I_{rq} + \frac{d\Psi_{rq}}{dt} \quad (2.61)$$

Similarly, the transformed flux linkage equations is given by:

$$\Psi_{sd} = L_d I_{sd} + L_{srd} I_{rd} \quad (2.62) \qquad \Psi_{rd} = \frac{3}{2} L_{srd} I_{sd} + L_{rd} I_{rd} \quad (2.64)$$

$$\Psi_{sq} = L_q I_{sq} + L_{srq} I_{rq} \quad (2.63) \qquad \Psi_{rq} = \frac{3}{2} L_{srq} I_{sq} + L_{rq} I_{rq} \quad (2.65)$$

The torque equation can be simplified significantly after transforming to the dq-reference frame. Using the Clarke and Park transformations, it can be shown that the physical equation for the electrical torque, Equation 2.37, simplifies to [35]:

$$T_e = \frac{3}{2} p(\Psi_{sd} I_{sq} - \Psi_{sq} I_{sd}) \quad (2.66)$$

$$= \frac{3}{2} p(\underline{I}_s^r)^T \mathbf{j} \underline{\Psi}_s^r \quad (2.67)$$

$$= \frac{3}{2} p \Psi_s I_s sin\phi_s^{\Psi_s} \quad (2.68)$$

Equation 2.68 shows that the electrical torque can be expressed as the vector product between the stator current vector and the stator flux linkage vector.

2.2.4 Per unit model

After transforming the physical equations to the dq-reference frame, they can be divided by the base value to get the per unit equations [34, p. 22]. Usually, the base values are based on the rated motor data. Then, it is easier to notice if the motor is overloaded. Moreover, scaling usually has to be done anyway when implementing controllers in a processor [35]. This section will present the per unit equations used in the Simulink model.

The per unit voltage equations are presented in Equation 2.69-2.73. As in the physical equations, the damper winding voltages are zero, because these windings are short-circuited.

$$u_d = r_s i_d + \frac{1}{\omega_n}\frac{d\psi_d}{dt} - n\psi_q \tag{2.69}$$

$$u_q = r_s i_q + \frac{1}{\omega_n}\frac{d\psi_q}{dt} + n\psi_d \tag{2.70}$$

$$0 = r_D i_d + \frac{1}{\omega_n}\frac{d\psi_D}{dt} \tag{2.71}$$

$$0 = r_Q i_Q + \frac{1}{\omega_n}\frac{d\psi_Q}{dt} \tag{2.72}$$

$$u_f = r_f i_f + \frac{1}{\omega_n}\frac{d\psi_f}{dt} \tag{2.73}$$

The flux linkages included in the per unit voltage equations, Equation 2.69-2.73, can be expressed as:

$$\psi_d = x_d i_d + x_{md}(i_D + i_f) \tag{2.74}$$

$$\psi_q = x_q i_q + x_{mq} i_Q \tag{2.75}$$

$$\psi_f = x_f i_f + x_{md}(i_D + i_d) \tag{2.76}$$

$$\psi_D = x_D i_D + x_{md}(i_d + i_f) \tag{2.77}$$

$$\psi_Q = x_Q i_Q + x_{mq} i_q \tag{2.78}$$

$$\tag{2.79}$$

By dividing Equation 2.66 with the base value, the per unit torque can be described by Equation 2.80.

$$\tau_e = \psi_{sd} i_{sq} - \psi_{sq} i_{sd} \tag{2.80}$$

2.2.5 Alternative per unit system

In order to have only measurable currents in the equations, an alternative set of per unit equations was obtained by Oddmund Grøvan in his Master thesis [19], and these equations were further modified by Magnus Bolstad in [10] and [11]. The alternative per unit equations were the basis of the Simulink structures used in the specialization project [29] and this master thesis. The final equations are summarized below, and the constants used in the equations are defined in Appendix C. The full derivation of the equations can be found in [10] and [11].

$$\begin{aligned} u_d = {} & r_d'' i_d + \frac{\sigma_d'' x_d}{\omega_n} \frac{di_d}{dt} - (1 - k_{fD}) \frac{r_{Rd}}{x_{Md}} \psi_{Rd} + (1 - k_{fD}) r_{Rd} i_f \\ & + k_{fD}(u_f - r_f i_f) - n\psi_q \end{aligned} \tag{2.81}$$

$$u_q = r_q' i_q + \frac{\sigma_{qQ} x_q}{\omega_n} \frac{di_q}{dt} - \frac{r_{Rq}}{x_{Mq}} \psi_{Rq} + n\psi_d \tag{2.82}$$

$$\begin{aligned} u_f = {} & r_f'' i_f + \frac{\sigma_f'' x_f}{\omega_n} \frac{di_f}{dt} - (1 - k_{dD}) \frac{r_{Rd}}{x_{Md}} \psi_{Rd} + (1 - k_{dD}) r_{Rd} i_d \\ & + k_{dD}(u_d - r_s i_d + n\psi_q) \end{aligned} \tag{2.83}$$

$$\frac{d\psi_{Rd}}{dt} = -\frac{\psi_{Rd}}{T_D} + \frac{x_{Md}}{T_D}(i_d + i_f) \tag{2.84}$$

$$\frac{d\psi_{Rq}}{dt} = -\frac{\psi_{Rq}}{T_Q} + \frac{x_{Mq}}{T_Q} i_q \tag{2.85}$$

$$\psi_d = x_d \sigma_{dD} i_d + \psi_{Rd} + x_{Md} \sigma_D i_f \tag{2.86}$$

$$\psi_q = x_q \sigma_{qQ} i_q + \psi_{Rq} \tag{2.87}$$

$$\psi_f = x_f \sigma_{Df} i_f + \psi_{Rd} + x_{Md} \sigma_D i_d \tag{2.88}$$

2.3 Control of the synchronous machine

The maximum torque per ampere ratio of a synchronous machine is obtained when the power factor is equal to one, i.e. when $cos\phi = 1$ [34]. This happens when the stator current and voltage are in phase. Starting from the condition that $cos\phi = 1$, it is possible to find the stator flux linkage that corresponds to the maximum torque per ampere.

The following analysis is based on [12], and is summarized in [34, p. 161]. If the stator resistance is neglected under steady-state conditions, the stator voltage equation reduces to:

$$u_s = jn\psi_s \tag{2.89}$$

From Equation 2.89, it can be observed that the stator voltage vector leads the stator flux linkage by $90°$.

In [13, p. 18], it is shown that the optimal pole wheel angle can be calculated as:

$$\delta = \frac{\tau_e x_q}{\psi_s^2} \tag{2.90}$$

To get the maximum Nm/A ratio, it can be observed from Equation 2.80 that the current in the d-axis i_{sd} should be zero and the stator flux linkage should be aligned with the d-axis. The torque equation then simplifies to:

$$\tau_e = \psi_s i_s \tag{2.91}$$

Equation 2.89 shows that to generate a voltage of 1 pu at 1 pu speed, a stator flux linkage of 1 pu is needed. To summarize, the machine should be controlled such that:

$$cos\phi = 1 \qquad \psi_s = 1 \tag{2.92}$$

An advantage of this control technique is that a lower current is handled by the converters [11]. This was especially important in the past when power converters were more expensive, and a converter with a lower power rating could be used to obtain the same torque.

In 1987, a control method named Direct Self Control was developed by Depenbrock in Germany [14]. This control strategy has later become known as DFLC, Direct Flux Linkage Control [37]. In this method, the stator flux linkage is controlled directly with the stator voltage vector, making current vector control unnecessary [37]. DFLC uses the voltage model to estimate the stator flux linkage, so the estimation relies on the stator resistance [37]. The main assumption of DFLC is that the voltage model alone can be used to estimate the stator flux linkage. This can, however, be difficult to achieve with high accuracy. Possible sources of error in the voltage model will be discussed in Section 3.1.1.

DTC, Direct Torque Control, is another control method where DFLC is combined with a supervising method (for example the current model), providing a more accurate flux linkage estimation at low speeds [32, 37]. The current model will be explained in more detail in Section 3.1.2. In DTC, the torque control and flux linkage control is combined, whereas other methods control these parameters in separate paths [37]. In [32], a method called DMCC (DLFC Modulater based Current Control), is presented. This method can be used at low speeds, making it suitable for sensorless control applications where a high torque is required at low speeds [32].

The synchronous machine in the Simulink model of this master thesis is current controlled. This is an indirect way of controlling the torque, hence its name ITC

(Indirect Torque Control). An advantage of this method is that the currents are controllable and stable. A disadvantage is that the position of the rotor is needed for the transformations. Consequently, DTC and DFLC are more popular for sensorless drives [11], as they lack the need for rotor position information.

For speed-controlled synchronous machines, the field weakening region is an important working area [37]. Field weakening is reached when the machine starts rotating above the rated speed. A voltage source inverter has a certain maximum voltage [37]. When the maximum voltage is reached, the flux linkage must be reduced to be able to increase the speed. This is usually done by applying a negative current in the d-axis [34]. Equation 2.89 shows that the stator flux linkage must be reduced inversely proportional to the speed [34]. In [11], simulations performed in Simulink showed that the current model was sensitive to field weakening. Field weakening of the synchronous machine has not been tested in the simulations of this master thesis.

2.4 PID controller

This section explains the function and main principles of a PID (Proportional Integral Derivative) controller. Tuning of PI controllers has been a focus area in this master thesis.

An ideal PID controller is given by Equation 2.93 [22], where u_0 is the manual control value, u is the input of the controller and e is the control error [23].

$$u = u_0 + K_p e_p + \frac{Kp}{T_i} \int_0^t e_i d\tau + K_p T_d \dot{e_d} \tag{2.93}$$

In the Laplace domain, the transfer function of an ideal PID controller can be written as [22, 39]:

$$h_{PID}(s) = K_p + \frac{K_p}{T_i s} + K_p T_d s \tag{2.94}$$

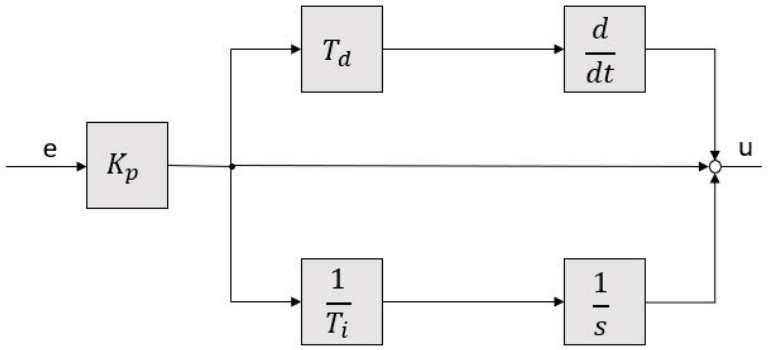

Figure 2.3: Block diagram of an ideal PID controller

Figure 2.3 shows a block diagram of an ideal PID controller. There are several different modifications of the ideal PID controller, but they all usually filter the derivative part using a low-pass filter [22]. One representation of a PID controller is described by Equation 2.95, where only the derivative term is filtered.

$$h_{PID}(s) = K_p + \frac{K_p}{T_i s} + \frac{K_p T_d s}{T_f s + 1} \tag{2.95}$$

Another option is to filter all the terms, i.e. the proportional, integral, and derivative term. This can be seen as a filter in series with an ideal PID controller.

$$h_{PID}(s) = (K_p + \frac{K_p}{T_i s} + K_p T_d s)\frac{1}{T_f s + 1} \tag{2.96}$$

A third representation is given by Equation 2.97. This is a multiplication of a PI and a PD controller, as if a PI and PD controller were in series. Equation 2.95 and 2.96 on the other hand are on a parallel form.

$$h_{PID}(s) = K_p \frac{(T_i s + 1)(T_d s + 1)}{T_i s(T_f s + 1)} \tag{2.97}$$

There are different ways to discretize the PID controller. The built-in discrete

PID controller block in Simulink used for the PI controller in the feedback loop of the closed-loop observer uses a parallel form where Equation 2.95 is discretized by the forward Euler method.

Chapter 3: Sensorless control

In this chapter, sensorless control of synchronous machines is explained and discussed. The concept of sensorless control and motivation for controlling the machine without sensors are explained in the following section. Then, flux models that can be used to estimate the rotor speed and position are presented in Section 3.1, including the well-known voltage model and current model. The final paragraphs of this chapter explain the drifting phenomenon, which is a result of stator flux linkage estimation errors.

Sensorless control is a term that describes the control of the machine without measurement of speed or rotor position. However, currents and voltages can be measured, so the system is not entirely sensorless. There are several advantages of sensorless control. The rotor position measurement is more expensive and fault sensitive than the current measurements [15]. In addition, the use of position sensors is not possible in some applications due to harsh conditions or lack of space [15, 28]. As sensorless control methods avoid the need for a tachometer, they offer advantages in cost and mechanical robustness [15, 21]. According to [9], the main problem of a position sensor is not the cost, but rather the reliability and consequent money loss due to downtime when there are faults on the sensor. Sensorless control methods also offer increased reliability and less space required [35, p. 217]. The complexity and maintenance requirements can be reduced by avoiding a position or speed sensor, and the drive's noise immunity increases [32]. Moreover, since the current and voltage sensors can be located with the control electronics and not adjacent to the machine, the sensors do not restrain the operating temperature [2].

3.1 Estimation of the stator flux linkage

Control of the synchronous machine requires information about the currents and rotor position [15]. In sensorless control methods, the rotor position can be estimated by using the stator flux linkage. Sensorless control using the flux linkage variation has been a well-known method for years, but has only been successfully implemented in the last couple of decades, when devices with enough real-time processing power have become available [2]. There are numerous ways to estimate the stator flux linkage, and some of these are covered in this section, most notably the current model and the voltage model. A combination of the voltage and current model was tested in Simulink in the specialization project, proving to improve the performance of the machine. This estimation method has been improved and tested more thoroughly in this master thesis.

3.1.1 Voltage Model

The so-called voltage model is one way to estimate the stator flux linkage. In the voltage model the measured stator current and voltage are utilized for the estimation of the stator flux linkage. The voltage model for stator flux linkage estimation is based on Equation 3.1:

$$\psi_s = \int_0^t (u_s - r_s i_s) dt \tag{3.1}$$

This equation is obtained by integrating Equation 2.2 and solving for the stator flux linkage, ψ_s. Then, a continuous estimation of the stator flux linkage can be produced by subtracting the resistive voltage drop from the stator voltage and integrating [2]. As the integration in Equation 3.1 is performed in the stationary reference frame, it is evident that the voltage model is independent of the rotor position. For this reason, the voltage model is often used for sensorless control. If all parameters in Equation 3.1 are estimated or measured with high accuracy, the voltage model estimates the stator flux linkage with high accuracy. However, the voltage model also has some disadvantages. A well-known problem for the voltage model is the performance at low speeds [2, 35], as Equation 3.1 will become an

open integrator at zero speed. The position estimate will thus vanish at low speeds [15]. Small measurement errors of the voltages and currents in Equation 3.1 will be integrated up and can cause large estimation errors [35]. An erroneously estimated stator resistance will have the same impact. According to Acarnley and Watson [2], it is not practical to measure the phase voltages in most electrical machines, because of isolation issues. Instead, the phase voltage is estimated by the DC supply voltage. This introduces measurement errors due to the dead-time of the converter. At low speeds, both the voltage drop across the stator resistance r_s and the inverter are of comparable size to the stator voltage, leading to inaccurate estimations [5]. Errors in the voltage model can lead to the drifting phenomenon, which will be covered in Section 3.1.4. The estimation errors of the open-loop integration in Equation 3.1 have driven research towards closed-loop stator flux linkage estimation methods [2], which will be presented in Chapter 4.

3.1.2 Current Model

Another way to estimate the stator flux linkage is the current model, first introduced by Blaschke [7] in 1972 [5]. The current model utilizes the currents to estimate the stator flux linkage, as the name suggests. Because current measurements are already needed for torque estimation, they can also be used to estimate the stator flux linkages [37]. First, the flux linkages of the d- and q-axes, ψ_d and ψ_q, are estimated using the currents i_d, i_q and i_f:

$$\psi_d = x_d \sigma_{dD} i_d + \psi_{Rd} + x_{Md} \sigma_D i_f \tag{3.2}$$

$$\psi_q = x_q \sigma_{qQ} i_q + \psi_{Rq} \tag{3.3}$$

Then, the estimated stator flux linkage can be defined as:

$$\psi_s = \psi_d + j\psi_q, \tag{3.4}$$

Equation 3.2 and 3.3 shows that the current model is relying on the accuracy of the estimation of the inductances. However, the inductances are generally easier to estimate than the stator resistance, since they only depend on saturation [35]. The inductances can be identified during start-up, and later be looked up in tables or

found using functions during operation [35, p. 216].

The flux linkages in the damper windings, ψ_{Rd} and ψ_{Rq}, can be calculated through Equation 2.84 and 2.85, repeated here for convenience:

$$\frac{d\psi_{Rd}}{dt} = -\frac{\psi_{Rd}}{T_D} + \frac{x_{Md}}{T_D}(i_d + i_f) \tag{3.5}$$

$$\frac{d\psi_{Rq}}{dt} = -\frac{\psi_{Rq}}{T_Q} + \frac{x_{Mq}}{T_Q} i_q \tag{3.6}$$

Whereas the voltage model does not need information about the rotor position or speed, the current model needs this information, either through estimation or measurement. This is because the calculations are performed in the rotating dq-reference frame, where information about the rotor position or speed is needed. A method for estimating the rotor speed and position is provided in Section 3.1.3. The current model does not involve any integrations, so it avoids the errors at low frequencies and the DC drifting problems of the voltage model [24]. If the parameters of Equation 3.2-3.6 are unknown or vary because of magnetic saturation or heating, the stator flux linkage estimate of the current model becomes incorrect [5].

3.1.3 Estimation of the rotor speed and position

How to estimate the rotor position and speed will be briefly explained in this section. A more thorough explanation is provided in [17] and [32], and the method is also summarized in the specialization project and master thesis of Magnus Bolstad [10, 11]. This way of calculating the rotor position has been implemented into the Simulink model in [11]. Figure 3.1 shows the relationship between the different space vectors used for the calculations. Using the figure, the rotor position angle, θ, can be calculated using trigonometric functions.

The figure shows a relationship between the rotor position, the position of the stator flux linkage, and the position of phase a of the stator voltages:

$$\theta = \varepsilon_s^s - \varepsilon_s^r \tag{3.7}$$

An implicit equation for the stator flux linkage can be derived through the use

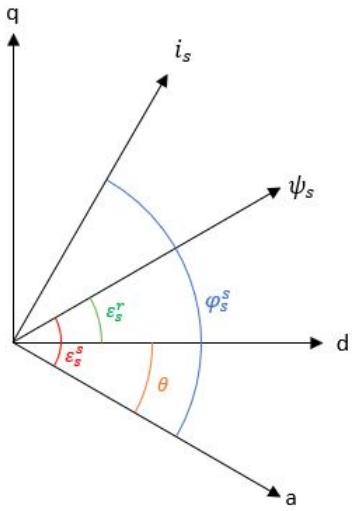

Figure 3.1: Space vector diagram showing the relationship between different angles

of trigonometric identities and Equation 2.85:

$$sin(\varepsilon_s^s - \theta) = \frac{\sigma_{qQ} x_q + \frac{x_{Mq}}{1+T_Q s}}{\psi_s} i_s sin(\varphi_s^s - \theta) \tag{3.8}$$

The full derivation of this equation can be found in [10], and is summarized Appendix A. The speed of the rotor can be found through Equation 3.9, using the definition of the derivative. Since the sampling time, T_{samp}, is important for the accuracy of the speed estimation, a low-pass filter has been added to the Simulink model [10, 17]. The low-pass filter provides a smoother speed response, at the cost of a small delay [9].

$$\hat{\omega}[k] = \frac{\hat{\theta}[k] - \hat{\theta}[k-1]}{T_{samp}} \tag{3.9}$$

The rotor position angle is initialized to a known angle during startup, i.e. $\theta = 0$. In the Simulink model, this was done by setting the rotor position to zero while the d-axis current reference was set to a constant value.

3.1.4 Drifting

The phenomenon called drifting occurs when inaccurate estimations and measurement errors cause the flux linkage vector to drift away from the origin [10]. The errors cause an oscillating stator flux linkage amplitude, which is illustrated in Figure 3.2a. The black circle shows the path of $\vec{\Psi}_s$ as the rotor rotates, while the red circle shows the path of the estimated flux linkage that has drifted away from the origin. Because the red circle is not centered at the origin, this will cause an oscillating stator flux linkage amplitude as the motor rotates. If the estimation is corrected, the stator flux linkage amplitude will stop increasing but will still have an offset to the actual stator flux linkage. This is also illustrated by Figure 3.2b, showing an example of drifting from the Simulink model. The figure shows the actual stator flux linkage, red, and the estimated stator flux linkage, blue, in the $\alpha\beta$ coordinate system. In the simulation, the stator flux linkage was underestimated ($\hat{r}_s = 0.6r_s$) for the first 0.9 seconds of the simulations, before it was corrected to the actual value. After the correction, the stator flux linkage amplitude is still erroneously estimated, even if the circles have the same radius, because the blue circle is not origin-centered. This leads to an oscillating amplitude error.

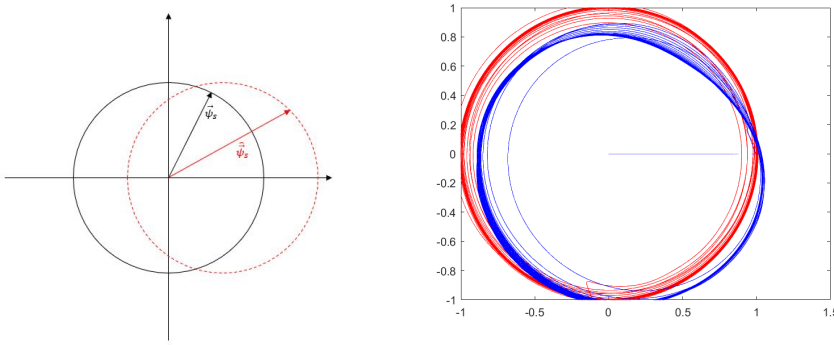

(a) Illustration of the drifting principle

(b) An example of drifting from the Simulink model

Figure 3.2: Drifting

There can be various causes of stator flux linkage drifting. Inaccurate estimations or measurements of the parameters in the voltage model is one cause. Another cause of drifting is errors in the initial conditions of the integral. Both an inaccurately

estimated stator resistance and a DC offset applied to one the stator voltages are tested in Simulink in this master thesis. Ways of correcting drifting will be presented and discussed in the next chapter.

Chapter 4: Improvement of the stator flux linkage estimation

This chapter explains how the stator flux linkage estimation can be improved. As discussed in Chapter 3, an inaccurately estimated stator flux linkage will lead to inaccurate estimations of the rotor position and speed, which will reduce the performance of the control. Different correction methods will be presented and explained in this chapter, with the main focus being on the combination of the current model and voltage model presented in Section 4.2. This method involves a PI controller that is used in the feedback loop. However, explanations of the combination method with a P controller is also provided, as this gives a more intuitive explanation of how the method works. In the specialization project [29], both a PI and a P controller were tested in the MATLAB/Simulink environment. A PLL has also been used to filter the rotor position that is input to the current model, and this concept is explained in Section 4.3. The main goal of the proposed correction methods is to get an estimation method that is less sensitive to estimation and measurement errors. Open-loop flux observers cause magnitude and phase errors at low frequencies [24], as discussed in Section 3.1.4. In order to avoid these problems, closed-loop observers are often used for sensorless control [24].

Section 4.1 explains the Niemelä method for drifting correction. In Section 4.2, the combination of the voltage model and the current model with a PI controller in the feedback loop is presented. This is the correction method that has been used in the simulations in this Master thesis, and a PLL was also added to improve the estimations even further. In the last section of this chapter, other drifting correction methods will be briefly explained.

4.1 Niemelä Method

The Niemelä method for flux linkage drifting correction was presented in [32]. The method was also discussed in [11], where it was referred to as "the method based on the square of the stator flux linkage". The Niemelä method is based on Equation 4.1:

$$e = \hat{\psi}_{s,LPF}^2 - \hat{\psi}_s^2 \tag{4.1}$$

The error signal e is defined as the difference between a squared low-pass filtered flux linkage estimation, and the same squared flux linkage estimation, but without the low-pass filter. The squared flux linkages peak simultaneously but in the opposite direction. The error signal will thus compensate and drive the stator flux linkage towards the actual value [11].

The corrected estimate of the stator flux linkage can then be described by the following equation:

$$\underline{\hat{\psi}}_s[k+1] = (1 + k_{\psi_{corr}} e)\underline{\hat{\psi}}_s[k] \tag{4.2}$$

Magnus Bolstad tested this correction method in [11, p. 62], and concluded that it works better for errors due to an erroneously estimated stator resistance than for voltage measurement offsets. The Niemelä method has not been tested in this master thesis.

4.2 Combination of the Voltage Model and Current Model

Another possible correction method is to combine the voltage model and the current model. As mentioned in Section 3.1.1, the main drawback of the voltage model is that the behavior at low-speeds is unsatisfactory [4, 38]. The current model, on the other hand, performs adequately at low speeds. The idea is to combine these methods by using the current model at low speeds and then smoothly transition to the voltage model as the speed increases. This closed-loop observer is able to

correct for errors due to both erroneous stator resistance and integrated DC voltage offsets [11, 27].

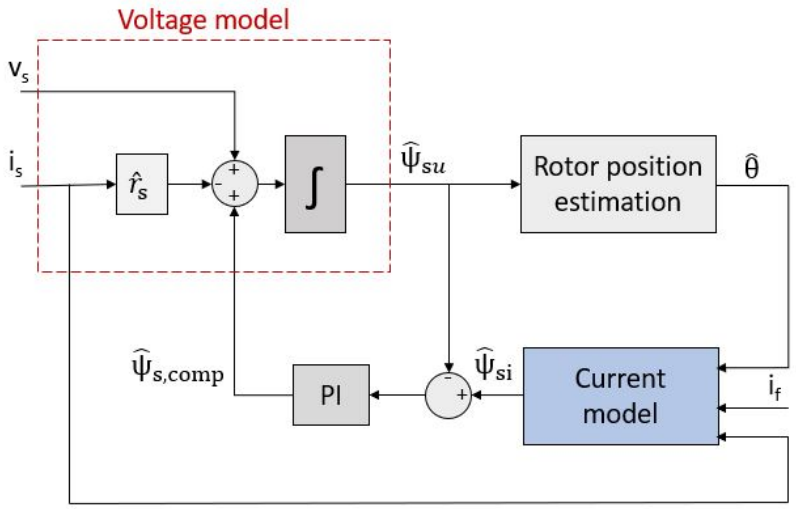

Figure 4.1: Block diagram illustrating the combination of the voltage model and current model with PI feedback

Figure 4.1 shows a block diagram that illustrates the combination of the voltage model and the current model, inspired by the figure presented in [11]. The estimated stator flux linkage from the voltage model, $\hat{\Psi}_{su}$ is used to estimate the rotor position that is input to the current model. The difference between the stator flux linkage estimates from the voltage and current model is sent back in a feedback loop through a PI controller. The output of the PI controller is a compensating term that returns as input to the voltage model. The voltage model can now be described by the following equation:

$$\psi_s = \int_0^t (u_s - r_s i_s + \psi_{s,comp}) dt \tag{4.3}$$

The same equation is used for the active flux observer presented in [9].

In order to explain the transition between the voltage model and the current model, a block diagram similar to the one in [31, p. 36] was made in the specialization project [29]. Figure 4.2 shows the simplified block diagram.

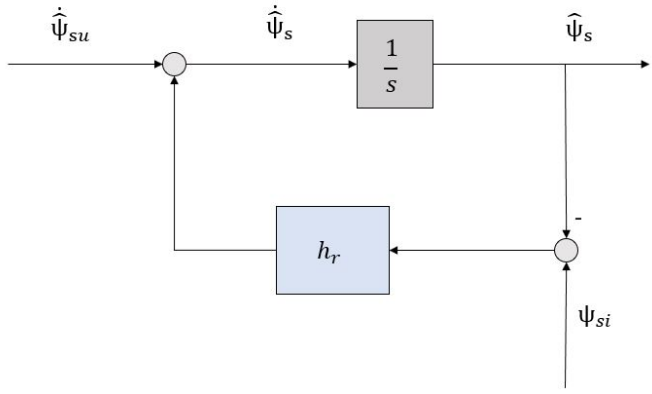

Figure 4.2: Block diagram illustrating the combination of the voltage model and current model with a P or PI controller in the feedback loop

It is possible to obtain a relationship between the estimated stator flux linkage from the voltage model and the current model using Figure 4.2. The stator flux linkage that is estimated by the current model is called ψ_{si}, while ψ_{su} denotes the stator flux linkage estimated by the voltage model.

The resulting stator flux linkage estimate, $\hat{\psi}_s$, can be described by Equation 4.4. The transfer function of the controller is defined as h_r. In the specialization project, both a P and a PI controller was tested in this feedback loop. The results found in the specialization project showed that the PI controller was able to improve the estimation accuracy, especially for drifting correction due to a DC offset in the voltage measurements [29].

$$\dot{\hat{\psi}}_s = \dot{\hat{\psi}}_{su} + h_r(\hat{\psi}_{si} - \hat{\psi}_s) \tag{4.4}$$

Equation 4.4 is in the time domain. Using the Laplace transform, this equation

can be transformed to the frequency domain. The new equation becomes:

$$\hat{\psi}_s s = \hat{\psi}_{su} s + h_r(\hat{\psi}_{si} - \hat{\psi}_s) \tag{4.5}$$

As previously mentioned, the PI controller in the feedback loop was able to improve the estimations of the stator flux linkage and rotor position in [29], and for this reason, only a PI controller has been used for the simulations in this master thesis. However, the concept of the combination method is easier explained using a P controller. The transfer function of a P controller is given by Equation 4.6, and the transfer function of a PI controller is given by Equation 4.7.

$$h_{r,P} = K_p \tag{4.6}$$

$$h_{r,PI} = K_p \frac{1 + T_i s}{T_i s} \tag{4.7}$$

The transfer function for the combination method with a P controller in the feedback loop is presented in Equation 4.8. This equation can be found by solving Equation 4.5 for the estimated stator flux linkage, $\hat{\psi}_s$, and inserting $K_p = \frac{1}{T}$.

$$\hat{\psi}_s = \frac{Ts}{1 + Ts}\hat{\psi}_{su} + \frac{1}{1 + Ts}\hat{\psi}_{si} \tag{4.8}$$

From Equation 4.8, it is evident that the term multiplied with the stator flux linkage estimated by the current model is a low-pass filter, and the term multiplied with the voltage model estimate is a high-pass filter. The combination method will consequently be able to rely on the current model for low-speed operation, where the voltage model provides inaccurate estimations [31]. As the speed increases, the machine can transition to using the voltage model, providing improved performance.

Using a PI controller in the feedback loop has been suggested in the literature to improve the performance of the estimations, and subsequently the sensorless operation [8, 9, 11, 27, 30]. According to [27, p. 554], the PI controller is able to eliminate DC offsets and drifting terms from measurements and from the initial conditions of the integrator.

The transfer function for $\hat{\psi}_s$ using the combination method with a PI controller

in the feedback loop can be written as:

$$\hat{\psi}_s = \frac{\frac{T_i}{K_p}s^2}{1 + T_i s + \frac{T_i}{K_p}s^2}\hat{\psi}_{su} + \frac{1 + T_i s}{1 + T_i s + \frac{T_i}{K_p}s^2}\hat{\psi}_{si} \tag{4.9}$$

This equation can be obtained in a similar way as for the P controller, but with $h_r = K_p\frac{1+T_i s}{T_i s}$ instead of a simple gain. To obtain the values of K_p and T_i, this expression can be compared to a general second-order transfer function. This process for tuning the PI controller will be explained in Chapter 5.

In this report, drifting correction due to a DC voltage offset has been tested in Simulink. The parameter sensitivity of the combination of the voltage and current model has also been analyzed and discussed.

4.3 Phase Locked Loop

To improve the model further, a phase locked loop (PLL) can be used to filter the rotor position that is input to the current model. This rotor position is estimated by the voltage model, as emphasized in Figure 4.1. The phase locked loop will act as a low-pass filter, and it is able to smoothen the estimated signal. The PLL is especially effective if the estimated signal oscillates around the actual one [11]. Figure 4.3 illustrates the phase locked loop as a block diagram. The illustration is inspired by the figure in [11, p. 91].

From Figure 4.3, the open-loop transfer function of the PLL can be identified as:

$$h_{PLL} = \frac{K_p\omega_n(1 + T_i s)}{T_i s^2} \tag{4.10}$$

The closed-loop transfer function of the PLL can then be written as:

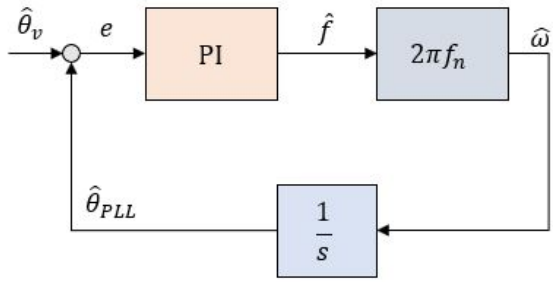

Figure 4.3: Block diagram illustrating the PLL

$$m_{PLL} = \frac{h_{PLL}}{1 + h_{PLL}} \tag{4.11}$$

$$= \frac{1 + T_i s}{1 + T_i s + \frac{T_i}{\omega_n K_p} s^2} \tag{4.12}$$

By comparing the denominator of Equation 4.12 with a general second-order transfer function like the one in [39, p. 205], the parameters T_i and K_p can then be found as:

$$T_i = \frac{2\zeta}{\omega_0} \tag{4.13}$$

$$K_p = \frac{T_i \omega_0^2}{\omega_n} = 2\zeta \frac{\omega_0}{\omega_n} \tag{4.14}$$

In [11], the phase locked loop block was successfully added to the Simulink model. The relative damping ratio, ζ, was set to 0.8. In this report, the PLL has been tested and compared to the performance of the closed-loop observer without PLL. In [11], a resonance frequency of $\omega_0 = 50$ rad/s showed the best performance. However, during testing in the specialization project [29], using a PLL caused larger overshoots in the simulations. Consequently, K_p and T_i have been tuned again in this master thesis, in an attempt to reduce these overshoots. The PLL has been tested for drifting correction due to an underestimated stator resistance, and DC offset in the voltage measurements. The results of these simulations

are presented in Section 7.2.4.

4.4 Other correction methods

In this section, some other ways to improve the accuracy of the stator flux linkage estimate will be presented. None of these methods have been implemented or tested in Simulink. One way to improve the combination of the voltage and current model is to compare the obtained values of ψ_{Rd} and ψ_{Rq} of the two methods, instead of comparing ψ_s. This method was suggested in [11], as ψ_{Rd} and ψ_{Rq} are filtered by the rotor time constants and change more slowly than ψ_s.

A method of position-sensing for a permanent-magnet synchronous machine (PMSM) was presented in [2], suggesting to use the inductance variation to estimate the rotor position. As the rate of current depends on the inductance of the winding, and the inductance is a function of the rotor position and winding current, the rotor position can be found using the winding current and its rate of change [2]. The advantage of this method is that it is able to operate also at low speeds. The challenge is to identify the initial position of the rotor. However, a salient-pole DC-excited synchronous machine has a small or even absent magnetic saliency of the rotor [9]. A similar observer to the one in this thesis is instead proposed for synchronous machines in [9], although the rotor position estimate is different.

Chapter 5: Tuning of the controllers

Different tuning methods for some of the controllers used in the simulation model are explained in this chapter. The results of these simulations are presented in Section 7.1, and are compared and discussed in Chapter 8. Section 5.1 explains how the field current controller can be tuned in order to follow the reference as accurately as possible. In Section 5.2, tuning of the PI controller of the closed-loop observer is presented. The same flux controller and stator current controller that were implemented in [11] have been used in the Simulink model in this thesis.

5.1 Field current controller

The field current controller was first implemented into the Simulink by Magnus Bolstad in [10]. Using the alternative per unit equation for the field voltage, Equation 2.83, it is possible to obtain a first-order differential equation relating the voltages and currents. The controller is tuned to handle the first-order transfer function, while the decoupling terms are fed forwarding to the controller output [10]. Bolstad tuned the field current controller through the use of modulus optimum, but symmetrical optimum was also suggested as a suitable tuning method.

Modulus optimum is a tuning technique that can be used when there is one large time constant and one or more smaller ones [35, p. 103]. The open loop of the transfer function can then be written on the form:

$$h_0(s) = K_p \frac{1 + T_i s}{T_i s} \cdot K_s \frac{1}{1 + T_{sum} s} \cdot \frac{1}{1 + T_1 s}, \tag{5.1}$$

where T_1 is the dominant time constant and T_{sum} is the sum of the smaller ones merged into one. It is then appropriate to select the time constant of the PI-controller equal to the dominant time constant, i.e. $T_i = T_1$, so that the far-right denominator in Equation 5.1 cancels out the numerator of the PI controller transfer function. Equation 5.1 can then be reduced to:

$$h_0(s) = \frac{K_p K_s}{T_1} \cdot \frac{1}{s(1 + T_{sum}s)} \tag{5.2}$$

The parameters of the PI controller can then be found as:

$$T_i = T_1 \tag{5.3}$$

$$K_p = \frac{T_1}{2K_s T_{sum}} \tag{5.4}$$

In the Simulink model, the controller parameters were implemented as functions of the machine parameters, so that the field current controller was tuned automatically if the machine parameters were changed. The tuning was based on Equation 5.5, which shows a relationship between the field voltage and the field current.

$$u_f = r_f^{"} if + \frac{\sigma_f^{"} x_f}{\omega_n} \frac{di_f}{dt} \tag{5.5}$$

The open-loop transfer function between the field voltage and field current can be described by the following equation [11]:

$$h_0 = \frac{i_f}{i_{f_{ref}}} = h_r \frac{i_f}{u_f} \tag{5.6}$$

Including the PI controller in the transfer function of the controller, h_r, this becomes:

$$h_0 = K_{p_f} \frac{1 + T_{i_f}s}{T_{i_f}s} \cdot \frac{1}{r_f^{"}\left(1 + \frac{\sigma_f^{"} x_f}{\omega_n r_f^{"}}s\right)\left(1 + T_{sum}s\right)} \tag{5.7}$$

Comparing this to Equation 5.1, it can be seen that the time constant T_{sum} is the sum of all the smaller time constants merged into one, and the dominant time constant in the system is $T_1 = \frac{\sigma_f'' x_f}{\omega_n r_f''}$. Using the modulus optimum criterion, it is possible to find the parameters of the PI controller as [11, 35]:

$$T_{i_f} = T_1 - \frac{T_{samp}}{2} = \frac{\sigma_f'' x_f}{\omega_n r_f''} - \frac{T_{samp}}{2} \tag{5.8}$$

$$K_{p_f} = \frac{T_1 - \frac{T_{samp}}{2}}{\frac{1}{r_f''}(2T_{sum} + T_{samp})} \tag{5.9}$$

The sampling terms are included in the above equations because the controllers are discretized [10, 35]. The decoupling terms used as a feed-forward compensation can be written as:

$$u_{f_{II}} = -(1 - k_{dD})\frac{\psi_D}{(1 + \sigma_D)\omega_n T_D} + (1 - k_{dD})\frac{r_D}{(1 + \sigma_D)^2} i_d \tag{5.10}$$

$$+k_{dD}(u_d - r_s i_d + n\psi_q) \tag{5.11}$$

$$= -(1 - k_{dD})\frac{r_{Rd}}{x_{Md}}\psi_{Rd} + (1 - k_{dD}) r_{Rd} i_d + k_{dD}(u_d - r_s i_d + n\psi_q) \tag{5.12}$$

These expressions are based on the alternative per unit voltage equation for the field voltage, Equation 2.83, repeated here for convenience:

$$\begin{aligned} u_f = r_f'' i_f + \frac{\sigma_f'' x_f}{\omega_n}\frac{di_f}{dt} - (1 - k_{dD})\frac{r_{Rd}}{x_{Md}}\psi_{Rd} + (1 - k_{dD}) r_{Rd} i_d \\ + k_{dD}(u_d - r_s i_d + n\psi_q) \end{aligned} \tag{5.13}$$

This method of tuning the field current controller was tested in Simulink, and the results are presented in Chapter 7.

This approach for tuning of the field current controller can also be found in [13], with a slightly different notation. In [13, p. 64], the control parameters are tuned based on what is referred to as ”betragsoptimum”. Similar to the modulus

optimum tuning method described in the previous section, the time constant is set to the value of the dominant time constant in the control loop:

$$T_{ne} = T_e \tag{5.14}$$

It can then be shown that the proportional gain should be set such that:

$$K_p = \frac{T_{ne}}{T_{ie}} = \frac{T_e}{2T_k u_{de0}} \tag{5.15}$$

By comparison with Equation 5.4, it can be observed that Equation 5.15 yields the same result when the open-loop transfer function of the converter has a gain of $K_s = u_{de0}$ and its delay is part of the sum of smaller time constants T_{sum}. The simulation results of the field current controller are presented in Chapter 7.

5.2 The PI Controller in the feedback loop

In this section, tuning of the PI controller in the feedback loop of the combination of the voltage and current model (explained in Section 4.2), will be presented and analyzed. Two different approaches have been used to tune the PI controller. In the specialization project [29], an experimental tuning method utilizing the nominal speed was used to tune the PI controller. This method is explained in Section 5.2.1. Another tuning strategy is the symmetrical optimum method, which is presented in Section 5.2.2.

5.2.1 Trial and error using the nominal speed

Through manipulation of the block diagram in Figure 4.2, it is possible to obtain a transfer function from the stator flux linkage estimation of the current model to the estimated stator flux linkage $\hat{\psi}_s$:

$$\frac{\hat{\psi}_s(s)}{\hat{\psi}_{si}(s)} = \frac{1 + T_i s}{1 + T_i s + \frac{T_i}{K_p \omega_n} s^2} \tag{5.16}$$

This expression can be compared to the second-order transfer function in [39, p. 205] to obtain the values of K_p and T_i. The denominator of a second-order transfer function is commonly written on the following form:

$$1 + 2\zeta\frac{s}{\omega_0} + (\frac{s}{\omega_0})^2 \tag{5.17}$$

Comparing this with Equation 5.16, T_i and K_p can be found as follows:

$$T_i = \frac{2\zeta}{\omega_0} \tag{5.18}$$

$$\frac{T_i}{K_p\omega_n} = \frac{1}{{\omega_0}^2} \implies K_p = \frac{T_i{\omega_0}^2}{\omega_n} \tag{5.19}$$

The nominal electrical speed can be written as $\omega_n = 2\pi f$. The tuning method used in the specialization project was to set ω_0 to 5, 10, and 15 percent of the nominal electrical speed, obtaining three of the values in Table 5.1. The relative damping ratio, ζ, was set to 0.7, and the frequency to 50 Hz.

	T_i	K_p
5%	0.0891	0.0700
7.5%	0.0594	0.1050
10%	0.0446	0.1401
12.5%	0.0357	0.1750
15%	0.0297	0.2099

Table 5.1: The values of T_i and K_p for ω_0 equal to 5, 7.5, 10, 12.5 and 15 percent of nominal speed

In this master thesis, additional tuning options of 7.5 and 12.5 percent were also added for a broader range of comparisons. Using the values in Table 5.1 as a starting point, the PI controller can be tuned by trial and error in Simulink. Drifting due to an underestimated stator resistance ($\hat{r}_s = 0.8r_s$) was tested in the specialization project, and in this master thesis drifting due to a DC offset in the voltage measurement has also been tested for tuning purposes. The results of these

tests are presented in Section 7.1.2.

5.2.2 Symmetrical optimum

Another way of tuning the controller is a method called symmetrical optimum. As there is an integrator in the process transfer function of the voltage model, it is not possible to cancel the numerator of the PI controller transfer function, as it is when using modulus optimum. For the symmetrical optimum, the closed-loop transfer function of the system can be obtained as [35, p. 104]:

$$M(s) = \frac{1 + T_i s}{1 + T_i s + \frac{T_1 T_i}{K_p K_s} s^2 + \frac{T_1 T_i T_{eq}}{K_p K_s} s^3} \tag{5.20}$$

$$= \frac{1 + \beta T_{sum} s}{1 + \beta T_{sum} s + \beta\sqrt{\beta} T_{sum}^2 s^2 + \beta\sqrt{\beta} T_{sum}^3 s^3} \tag{5.21}$$

K_p and T_i can then be chosen such that:

$$T_i = \beta T_{sum} \tag{5.22}$$

$$\omega_c = \frac{1}{\sqrt{\beta} T_{sum}} \tag{5.23}$$

$$K_p = \frac{T_1}{K_s \sqrt{\beta} T_{sum}} \tag{5.24}$$

$$|h_0(\omega_c)| = 1 \tag{5.25}$$

This ensures that the phase of the transfer function is lifted in the frequency range between $\frac{1}{\beta T_{sum}}$ and $\frac{1}{T_{sum}}$, with the largest phase margin occuring at $\frac{1}{\sqrt{\beta} T_{sum}}$ [35]. β set to 4 leads to a rise time of $T_{rise} = 3.1 T_{sum}$ and a settling time of $T_{settling} = 16.5 T_{sum}$ [35]. The overshoot however is as large as 43.4%. In this master thesis, $\beta = 4$ has been used in the Simulink model. The performance of the PI tuning using symmetrical optimum is shown in Chapter 7.

Chapter 6: Simulation model

This chapter presents the synchronous machine model that has been used in Simulink. The blocks of the outer layer of the Simulink model are explained, and the advantages of simulations rather than experimental testing are discussed. As the Simulink model is complex and has several layers, only the main parts will be explained in this chapter.

Sensorless control of a synchronous machine has been thoroughly tested in the MATLAB/Simulink environment in this Master thesis. The Simulink model that has been used was first made by Roy Nilsen, and later modified to apply for sensorless control of a synchronous machine by Bolstad in [10] and [11]. The model has been modified further by the author in the specialization project [29], and in this master thesis. The outer layer of the Simulink model is shown in Figure 6.1.

The three-phase stator voltages are supplied by a three-phase inverter that is PWM-controlled. A PWM-controlled DC-DC full bridge converter supplies the field voltage. The duty ratio of the full-bridge converter is obtained by a PI field current controller. The reference of the field current controller is determined by a PI flux controller, which has the aim of obtaining a stator flux linkage of 1 pu to obtain maximum Nm/A ratio [11], as discussed in Section 2.3. The duty ratio of the 3-phase 2-level inverter is determined by PI current controllers. The outer layer of the block ”SM control 3-phase” is presented in Appendix E.

The switching frequency of the PWMs is set to 3 kHz. The ode23tb solver in Simulink has been used, with the solver reset method set to robust. The maximum

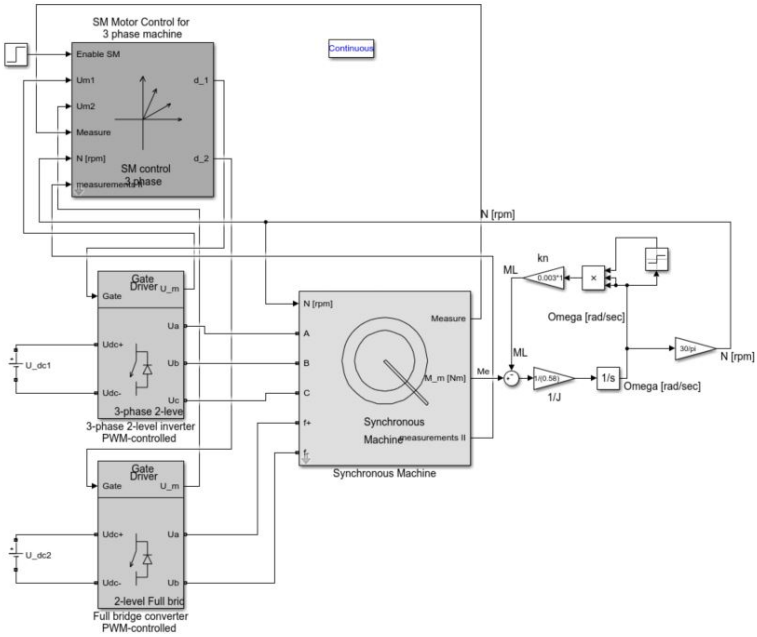

Figure 6.1: Outer layer of the Simulink model

step size was set to 100 μs. The blocks on the right-hand side of the synchronous machine in Figure 6.1 represent the mechanical load, which corresponds to typical pump characteristics. This can be described by Equation 6.1, where the constant k has been determined to give nominal power at nominal speed [11].

$$\tau_{load} = k\omega_{mech}^2 \tag{6.1}$$

One of the main advantages of simulations rather than experimental testing in the laboratory is that the actual values of the stator flux linkage, rotor position, and rotor speed are available for comparison. By comparing the results of the estimations to the actual values, possible sources of errors can be identified, and the model can be improved. A disadvantage is that the simulations are time-consuming, limiting the opportunity to test a wide variety of scenarios. In addition, the behavior

of a real synchronous machine is difficult to replicate in Simulink perfectly.

The machine parameters of the synchronous machine are listed in Appendix B. The control structure showing the combination of the voltage model and the current model with a PI controller is presented in Figure 10.5 of Appendix E.

Chapter 7: Simulation results

Results from the simulations performed in Simulink are presented in this chapter. First, tuning of the controllers is covered in Section 7.1, where the field current controller and the PI controller in the combination method have been tested. Then, the parameter sensitivity during sensorless control is investigated in Section 7.2. The parameter sensitivity includes testing of performance during errors in estimations or measurements of the stator resistance, damper winding resistance, and the inductances of the d- and q-axis. The accuracy of the stator flux linkage when a DC voltage offset is applied to one of the stator voltage phases is presented in Section 7.2.2.

7.1 Tuning of the controllers

The results of the tuning methods introduced in Chapter 5 are presented in this section. The results of the field current controller are given in Section 7.1.1, while tuning of the PI controller is addressed in Section 7.1.2.

7.1.1 Field Current Controller

In this section, simulation results of the field current controller tuning are presented. To test the field current controller in Simulink, a varying field current reference, $i_{f_{ref}}$, was used instead of the reference obtained from the flux controller. Figure 7.1 shows how the field current followed its reference when the controller was tuned with modulus optimum, similar to in [10]. The graph also shows the performance when the gain is doubled, which Bolstad suggested in [10]. When doubling the gain, the field current is able to follow the reference more accurately, but the drawback is the small overshoots. However, these overshoots are very small in

magnitude, so the value obtained by modulus optimum was doubled by Bolstad in his simulations.

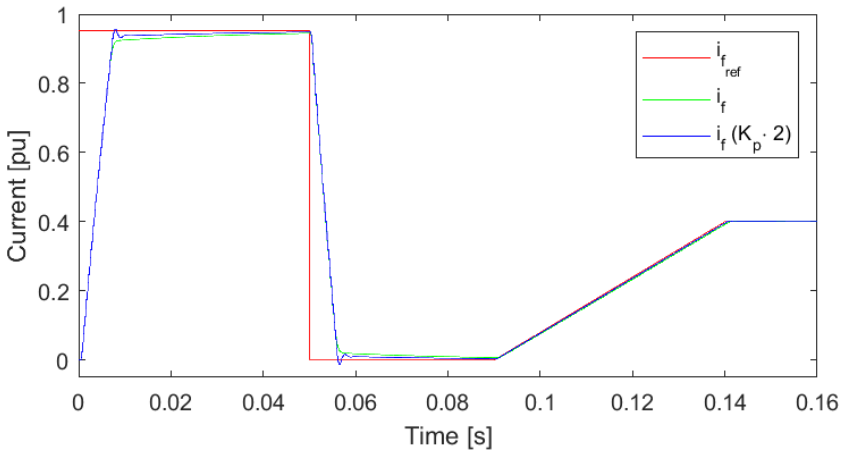

Figure 7.1: Field current controller tuned by modulus optimum

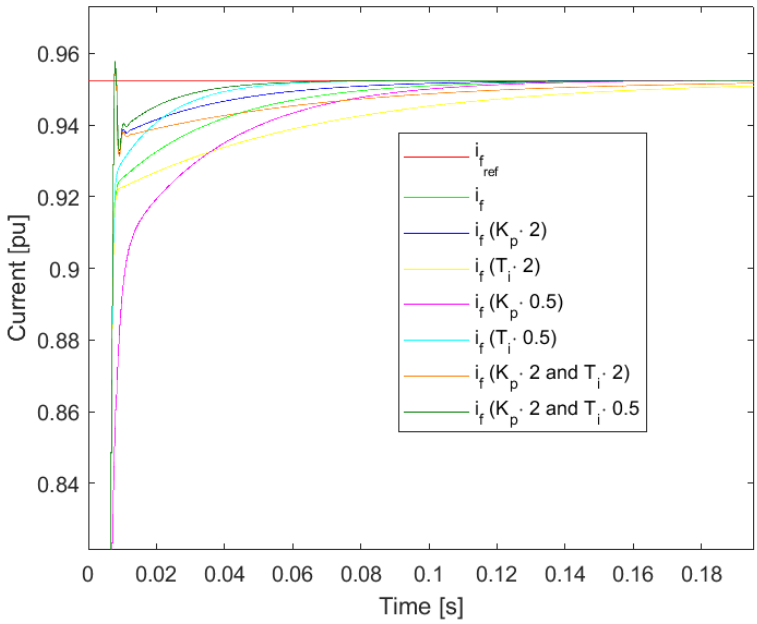

Figure 7.2: Zoomed in view at the overshoots of the field current controller. Light green is tuned by symmetrical optimum.

A Bode plot of the open-loop transfer function of the field controller, expressed in Equation 5.7, is shown in Figure 7.3. The orange curve shows the Bode plot from when the controller was tuned by modulus optimum, while the blue curve has the same T_i, but the gain is doubled. By doubling the gain, the bandwidth is increased, but the phase margin is slightly decreased, from $69.3°$ to $56.8°$. The phase margin is in both cases still within the typical requirement of $45°$.

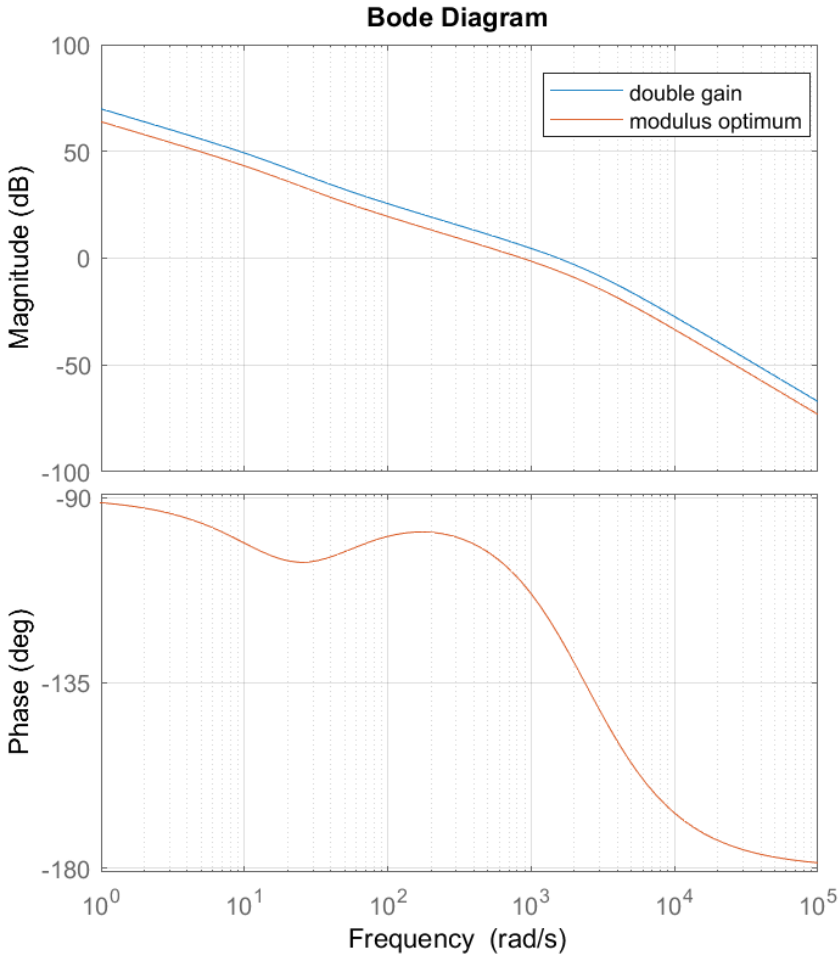

Figure 7.3: Bode plot of the open-loop transfer function of the field current controller

Figure 7.2 shows a zoomed in view at the overshoots, where the values of K_p and T_i have been changed in an attempt to follow the reference even faster. It is evident from the figure that by doubling the gain and halving T_i (the dark green curve), the field current follows its reference slightly faster, while the overshoot stays the same.

7.1.2 The PI Controller in the feedback loop

In this section, the results from the tuning of the PI controller in the feedback loop are presented. The first part of this section shows the results with a similar approach as in [29], and the second part presents the results obtained by symmetrical optimum.

Experimental tuning

Figure 7.4 shows the amplitude errors of the stator flux linkage for ω_0 tuned to 5, 7.5, 10, 12.5 and 15 percent of the nominal electrical speed when the stator resistance is underestimated ($\hat{r}_s = 0.8r_s$). Figure 7.5 shows the angle errors with the same tuning of the PI controller.

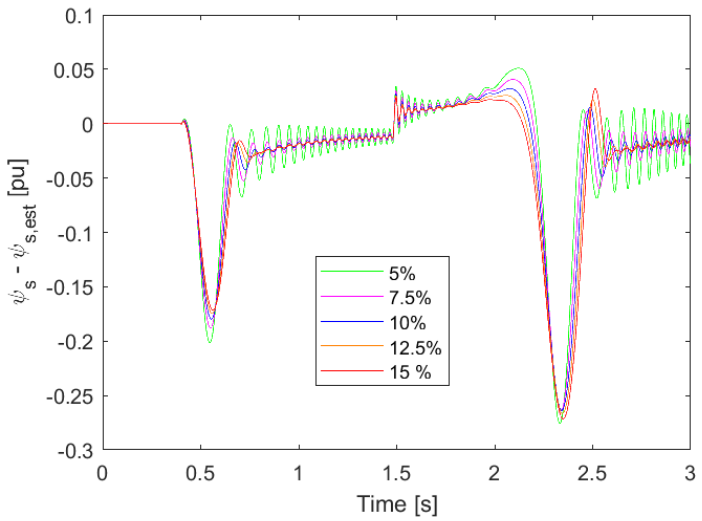

Figure 7.4: Stator flux linkage amplitude error, underestimated resistance

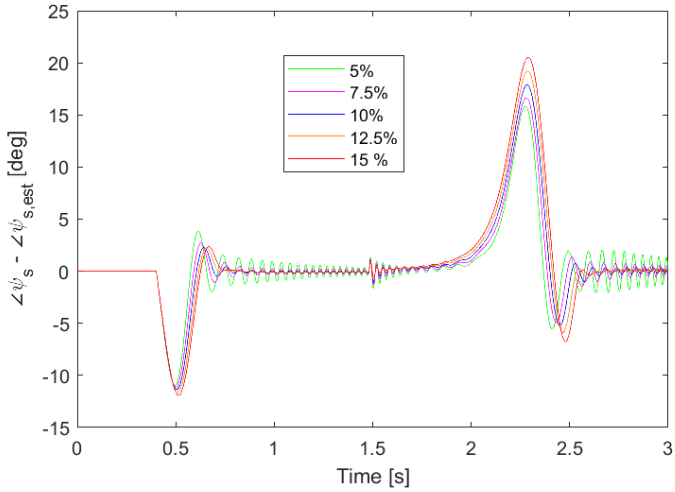

Figure 7.5: Stator flux linkage angle error, underestimated resistance

From Figure 7.4 and 7.5 it can be argued that ω_0 set to 12.5 percent of the nominal speed proves to be the tuning method with the most accurate stator flux linkage estimation. The overshoots are reasonably small, while it is still able to dampen the oscillations at higher speeds. Tuning K_p and T_i such that ω_0 is 10 percent of the nominal speed also shows good performance. The two lowest percentages, 5 and 7.5, provide small overshoots but the oscillations are quite large.

How the tuning of the PI controller impacts the accuracy of the stator flux linkage estimation was also tested when a DC offset of 2V was added to one of the stator voltage phases. Figure 7.6 and 7.7 show the stator flux linkage angle and amplitude error when the DC offset was applied. The Figures show that the 5 % tuning scenario actually provides the fastest drifting correction. This option makes the errors decrease rapidly, and even avoids noticeable overshoots when crossing zero speed. The PI tuned after 15 % of the nominal speed, on the other hand, starts with significantly smaller oscillations. However, the magnitude of the peaks remains at approximately the same value.

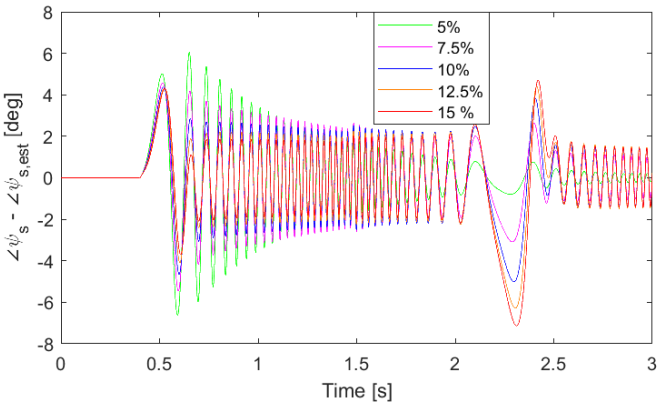

Figure 7.6: PI Tuning: Stator flux linkage angle error, DC offset in voltage measurement

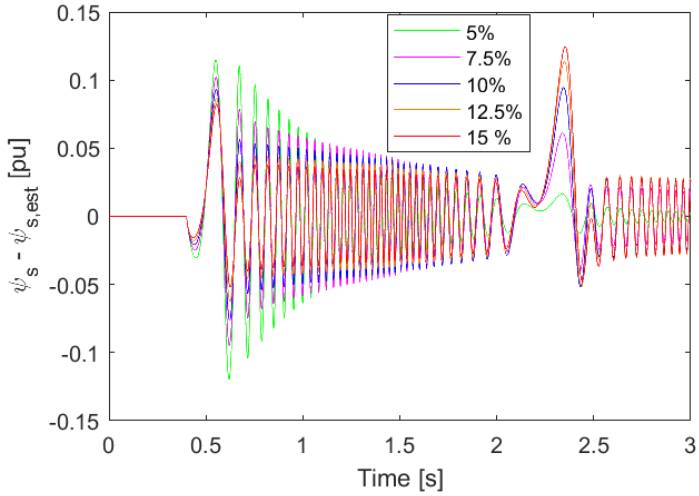

Figure 7.7: PI Tuning: Stator flux linkage amplitude error, DC offset in voltage measurement

Symmetrical optimum

The symmetrical optimum tuning strategy is suitable for tuning the PI controller in the feedback loop because of the integrator in the voltage model. Using the equations presented in Section 5.2.2, the values of the PI controller parameters can be found as:

$$T_i = 0.0020 \qquad (7.1) \qquad\qquad K_p = 0.1667 \qquad (7.2)$$

A Bode plot of the open-loop transfer function of the system is presented in Figure 7.8. The Bode diagram shows the characteristic phase lift of the symmetric optimum, and the largest phase margin occurs at about 1000 rad/s, which roughly corresponds to the theoretical value of $\frac{1}{\sqrt{\beta}T_{sum}} = 1200$.

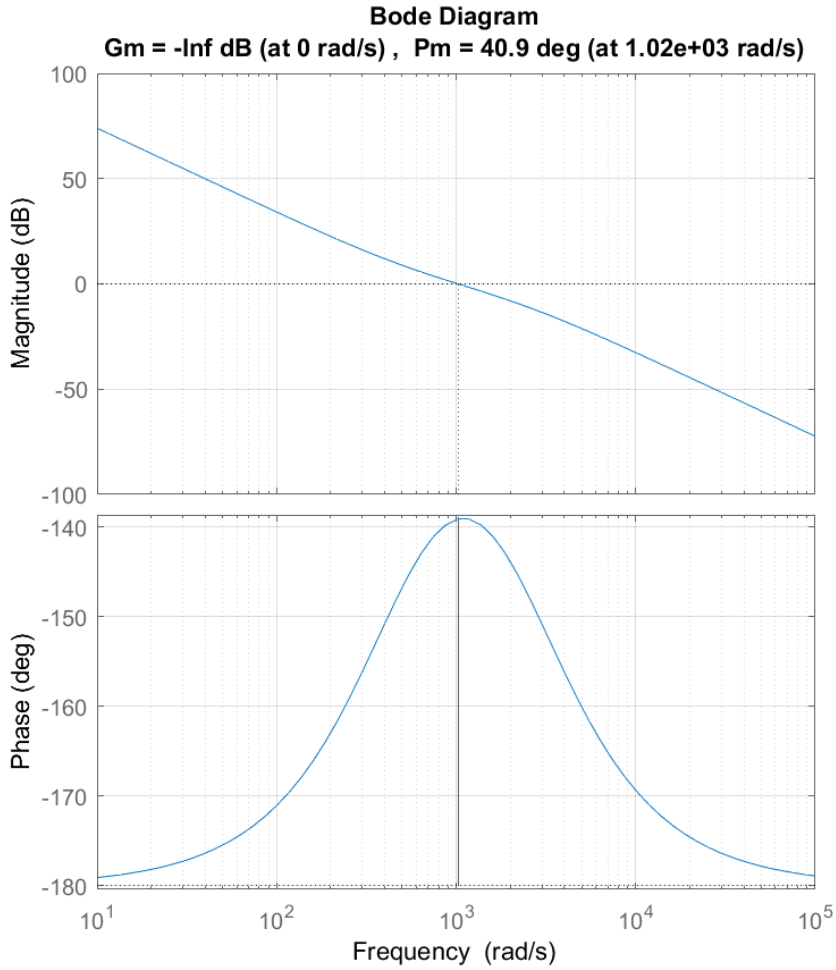

Figure 7.8: Bode plot of the open-loop transfer function of the combination method

Figure 7.9 shows that the stator flux linkage estimate is able to follow the reference with high accuracy, but with overshoots at start-up and when crossing zero-speed. Comparing the error curves to Figure 7.4 and 7.5, it is evident that although the overshoots are of approximately the same size, there are significantly fewer oscillations when using symmetrical optimum. In the following sections, the PI controller has been tuned by symmetrical optimum.

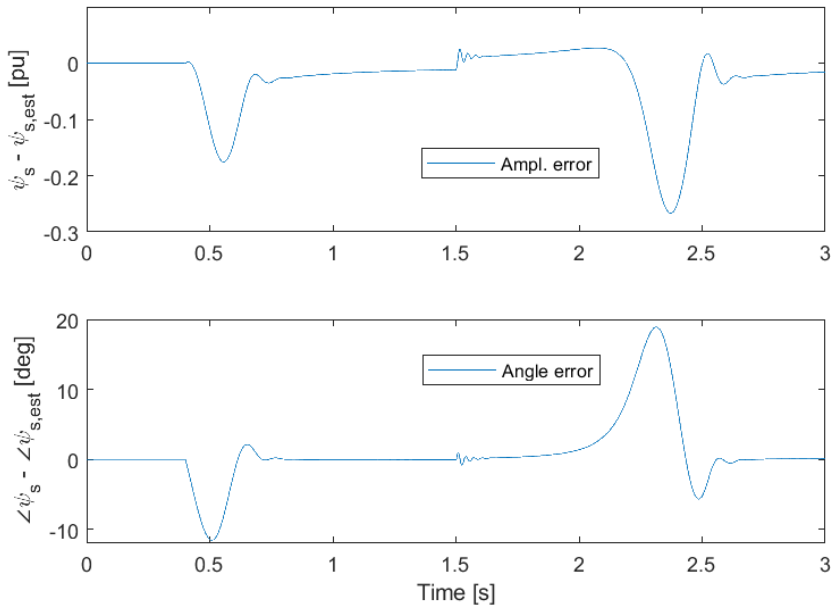

Figure 7.9: The amplitude and angle error when the PI controller was tuned by symmetrical optimum, $\hat{r_s} = 0.8r_s$

The amplitude and angle errors of the stator flux linkage when a DC offset was applied to one of the stator voltages is shown in Figure 7.10. The figure shows that tuning the PI controller by symmetrical optimum works better than the experimental method for drifting correction due to an underestimated stator resistance, but not when a DC voltage offset was applied. The error curves have peaks when the motor starts rotating and when crossing zero-speed just like Figure 7.6 and 7.7, but in between the peaks, the error curves are oscillating without getting dampened.

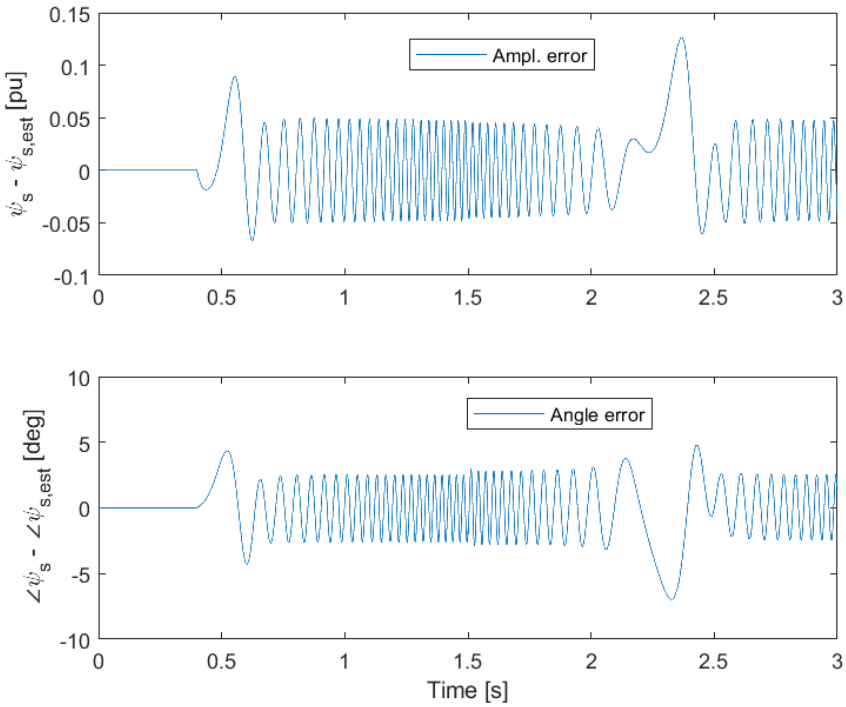

Figure 7.10: The amplitude and angle error when the PI controller was tuned by symmetrical optimum, 2V DC offset

7.2 Sensorless control of a synchronous machine

Sensorless control of a separately excited synchronous machine is investigated in this section. Section 7.2.1 tests how the accuracy of the stator flux linkage estimate depends on various parameters. In Section 7.2.2, the control system's ability to correct for drifting due to a DC offset in the voltage measurement is analyzed. In Section 7.2.3, the motor drives slower through zero-speed while the resistance is underestimated. Section 7.2.4 presents the results when using a PLL to filter the current model's rotor position input.

Figure 7.11 shows the stator flux linkage and rotor position errors when the stator resistance is underestimated by 20%, and no drifting correction method

is applied. The rotor position angle from the voltage model is used as input to the current model, but there is no feedback in the system, making this an open-loop observer. The graphs clearly show that after the torque reference is applied, the stator flux linkage errors are inaccurate, and they increase throughout the simulation time. Especially the stator flux linkage angle and rotor position angle errors are unacceptable, as they deviate more than $50°$ from the actual angle. Hence a correction method is needed, and the closed-loop observer combining the voltage model and current model is used in the rest of the simulations. In the following sections, how the different parameters affect the machine performance will be analyzed.

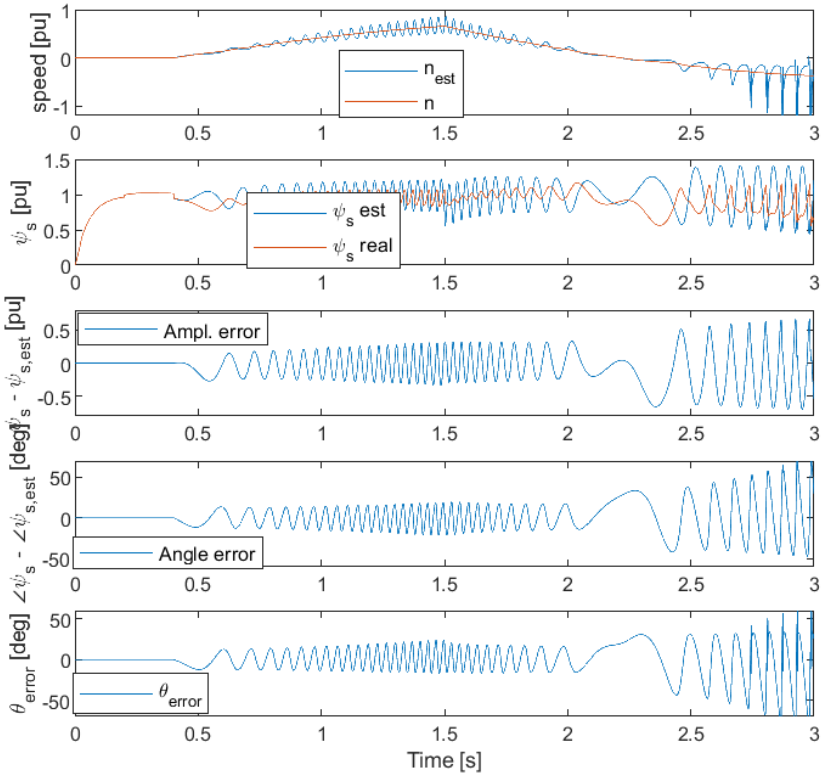

Figure 7.11: The estimation errors with an underestimated stator resistance ($\hat{r}_s = 0.8r_s$ without any correction method

7.2.1 Parameter Sensitivity

In the specialization project [29], an underestimated resistance was used in the simulations. This has also been done in this master thesis, with the addition of an overestimated resistance. The control method's sensitivity to errors in the d- and q-axis inductances and the resistances in the damper windings are also tested.

Stator resistance r_s

The voltage model is heavily dependent on the accuracy of the stator resistance, evident from Equation 3.1. In this section, the stator resistance has been under- and overestimated while running the machine in sensorless operation.

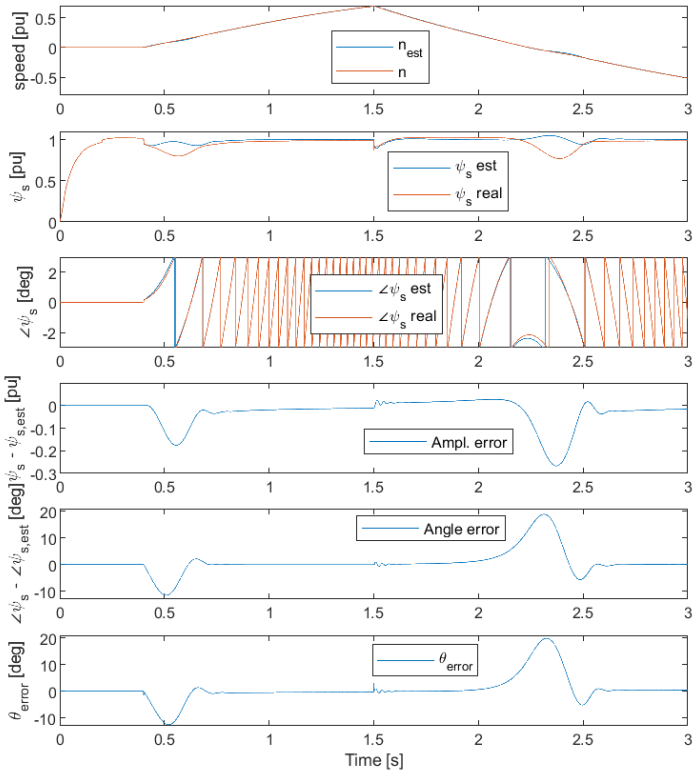

Figure 7.12: Underestimated stator resistance, $\hat{r}_s = 0.8r_s$

Figure 7.12 shows the results of a simulation where the stator resistance is underestimated, $\hat{r}_s = 0.8r_s$. The graphs show that both the stator flux linkage and rotor position are estimated with high accuracy, except at start-up and when crossing zero-speed. The maxima of the error curves occur after approximately 2.4 seconds. At this point, the amplitude error is almost 0.3 pu., while the stator flux linkage angle and rotor position deviate roughly 20° from the actual values.

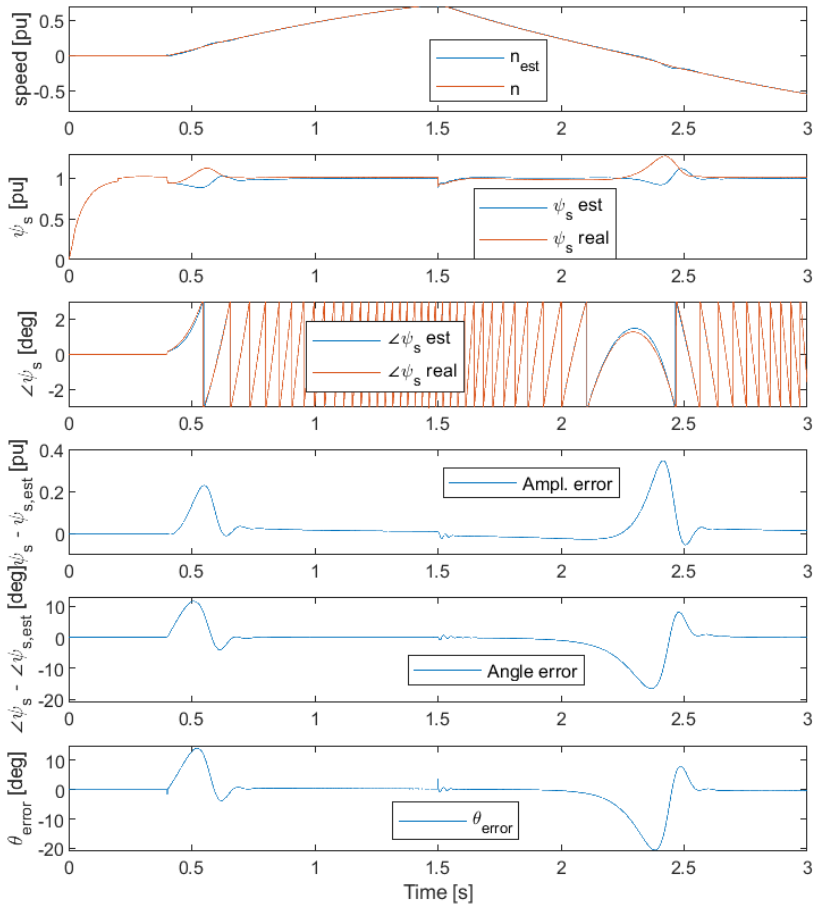

Figure 7.13: Overestimated stator resistance, $\hat{r}_s = 1.2r_s$

In Figure 7.13, the same simulation is done with an overestimated stator resistance,

$\hat{r}_s = 1.2r_s$. The graphs show the same curve as in Figure 7.12, but the peaks are in the opposite direction. The amplitude error when crossing zero-speed is slightly larger than when the stator resistance was underestimated.

Inductances x_q and x_d

In this section, how the inductances of the direct and quadrature axis affect the stator flux linkage and rotor position estimation is tested. Figure 7.14 shows the results of the simulations when x_q was under- and overestimated by 20%. The estimations errors at start-up are minimal, but still peak when crossing zero-speed. The rotor position angle estimate has a noticeable spike after 1.5 seconds when the torque reference is changed.

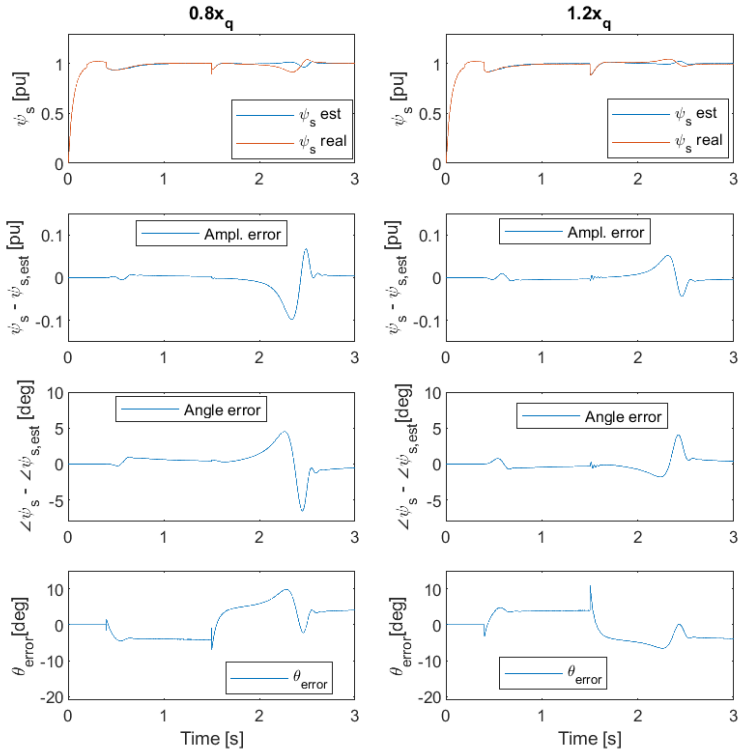

Figure 7.14: Underestimated (left) and overestimated (right) x_q

Then, x_q was set to its actual value, and x_d was under- and overestimated by

20%. The results of these simulations are shown in Figure 7.15. The underestimation of x_d leads to a low stator flux linkage amplitude error. The angle estimations, however, deviate significantly from the actual value, showing unacceptable estimation errors at low speeds. When x_d is overestimated by 20 %, it is evident from Figure 7.15 that something wrong happens in the simulation, as the actual stator flux linkage starts increasing towards 10 pu. This also happens if the machine runs with a position sensor.

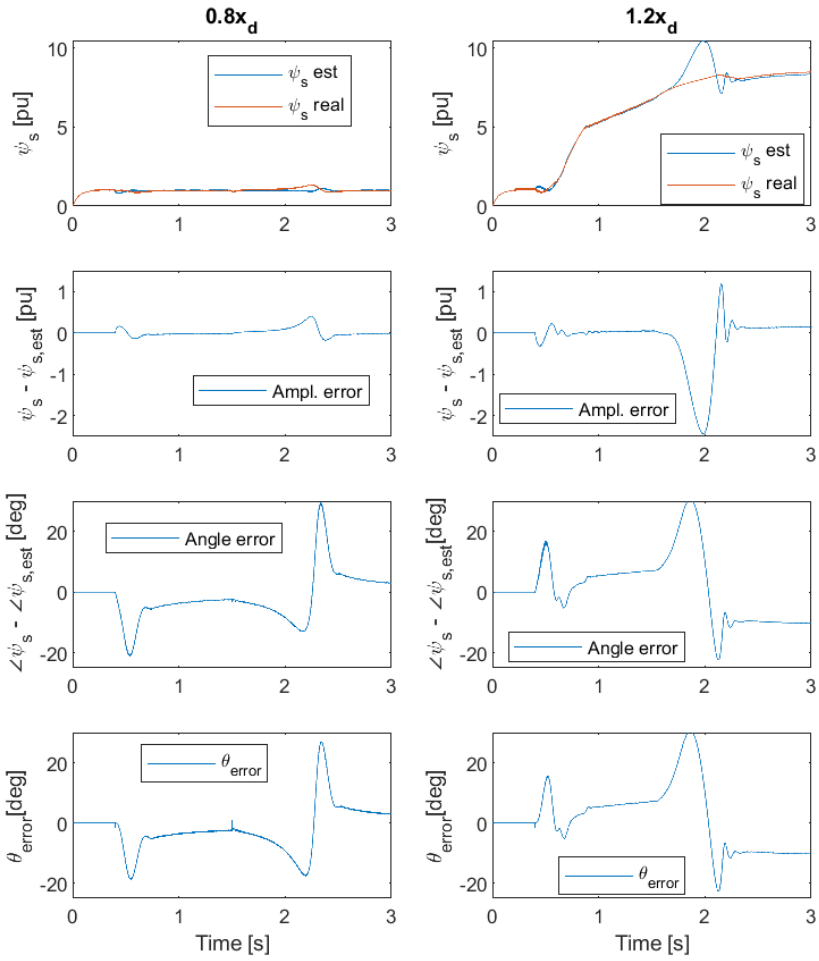

Figure 7.15: Underestimated (left) and overestimated (right) x_d

Resistance in the damper windings r_D and r_Q

Figure 7.16 shows the stator flux linkage and rotor position errors for an over- and underestimated damper winding resistance in the quadrature axis. The figure shows that the stator flux linkage angle and especially the amplitude are estimated with high accuracy. The rotor position angle errors are somewhat bigger and have a spike after 1.5 seconds when the torque reference changes from positive to negative.

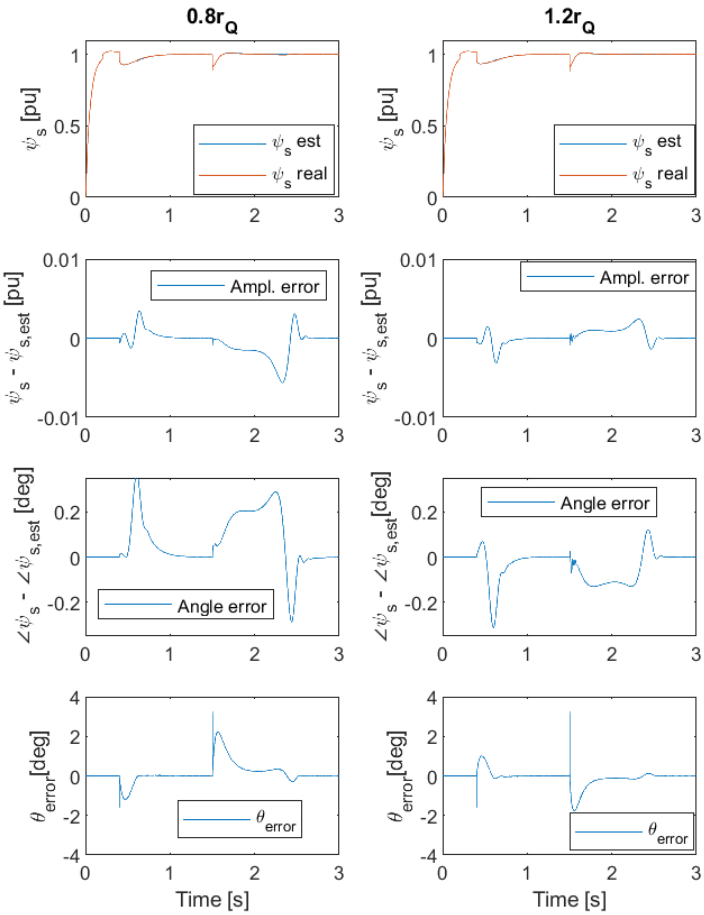

Figure 7.16: Underestimated (left) and overestimated (right) r_Q

The damper winding resistance in the direct axis, $\hat{r}_D$, was then estimated as $0.8r_D$ and $1.2r_D$. The results are presented in Figure 7.17. The error curves show that the while the amplitude errors are minimal, they are considerably larger than for erroneous estimation of r_Q. The stator flux linkage error is of a noticeably larger magnitude than for r_Q, and it oscillates throughout the simulation. The rotor position error shows a similar curve to that of Figure 7.16, but an oscillating behavior is still observed.

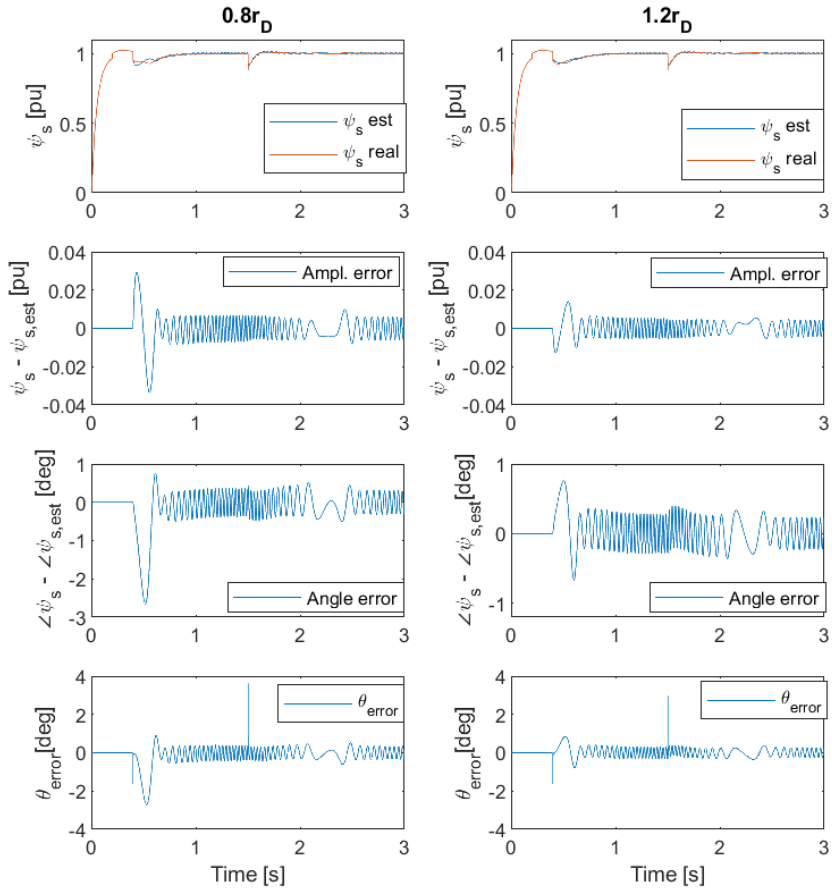

Figure 7.17: Underestimated (left) and overestimated (right) r_D

7.2.2 Voltage offset

In order to test how the control system is able to correct for errors in voltage measurements, a DC offset of 2V was added to one of the phases of the stator voltages. The same torque reference as in the other simulations was used, and the results of the simulation are presented in Figure 7.18. The figure shows that the stator flux linkage estimate oscillates around the actual value. Although the errors are larger at low speeds, the estimated stator flux linkage oscillates around the real value throughout the simulation.

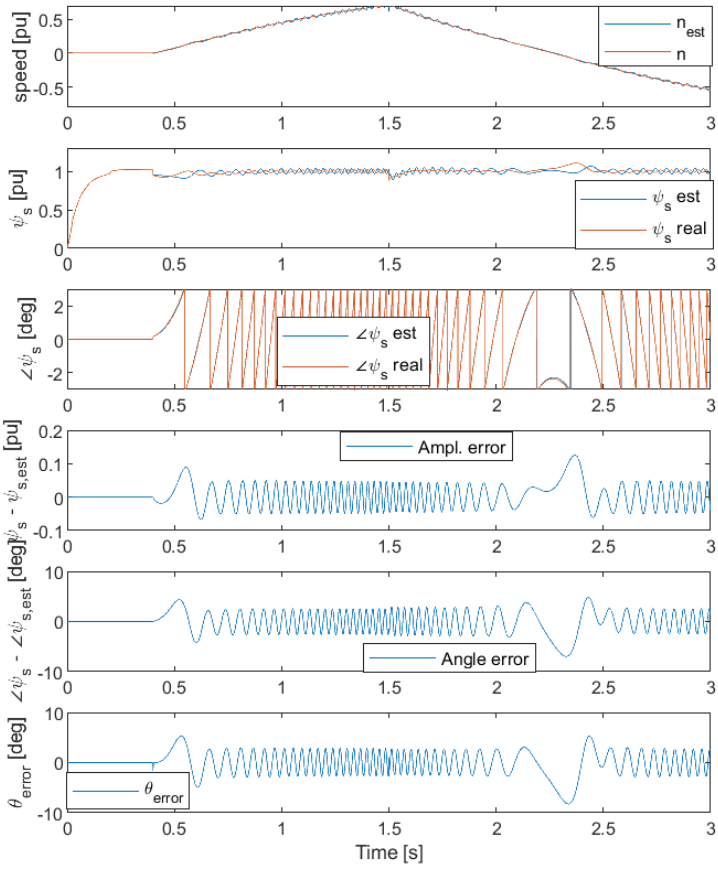

Figure 7.18: Sensorless control with a DC offset of 2V in voltage measurements

7.2.3 Driving slowly through zero speed

Until now, the zero-crossing has been relatively fast. In this section, a slower crossing of the zero-speed will be simulated. Figure 7.19 shows the results of a simulation where the stator resistance was underestimated, but this time for a longer time period (10 s) and with a slower deceleration through zero speed.

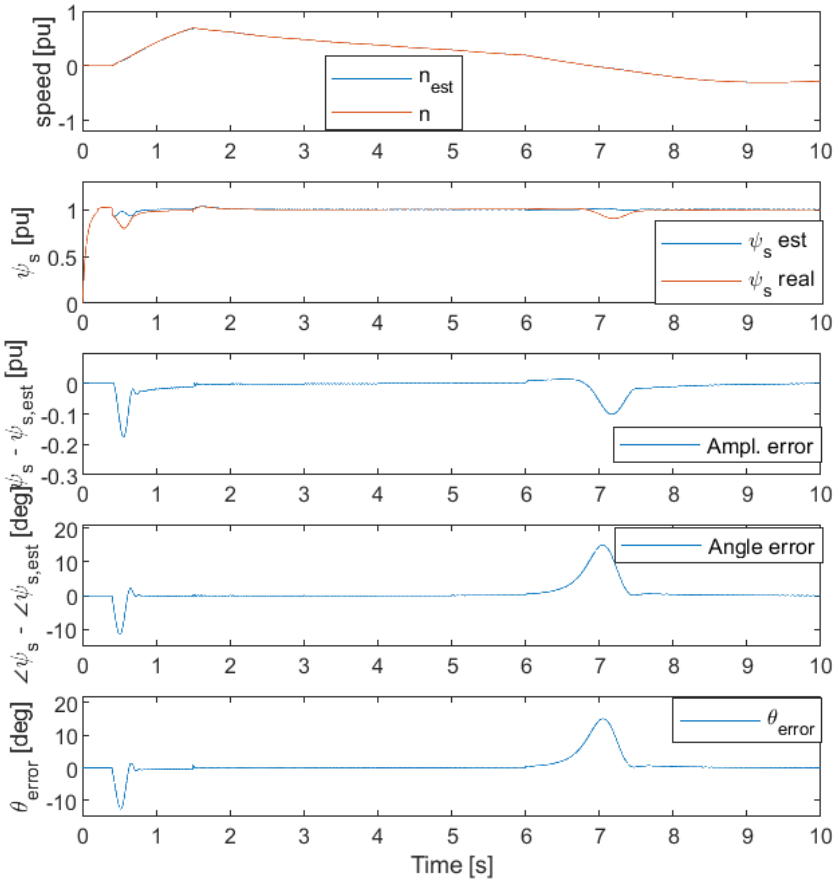

Figure 7.19: Driving slowly through zero-speed, $\hat{r}_s = 0.8r_s$

7.2.4 Phase Locked Loop

In order to improve the stator flux linkage and rotor position estimations, the PLL can be used to filter the rotor position that is input to the current model. In the specialization project, the PLL was able to reduce the estimation errors, but at the cost of larger overshoots at low speeds. In this section, the stator resistance has been underestimated by 20% while using a PLL. The PLL has also been used when a DC voltage offset was applied.

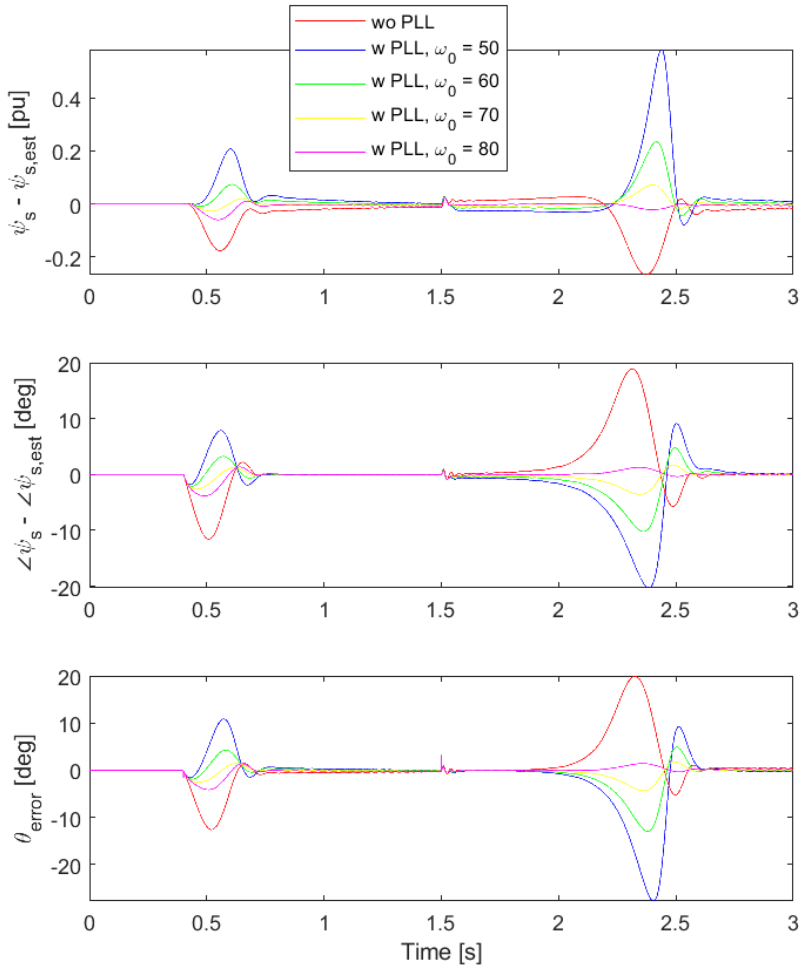

Figure 7.20: Estimation errors with and without PLL, $\hat{r}_s = 0.8r_s$

First, the PLL was used to reduce the estimation errors due to an underestimated resistance. The simulations in the specialization project [29], showed that by using a PLL, there were larger errors at low speeds than without. For this reason, the PLL has been tuned in this master thesis. Figure 7.20 shows the stator flux linkage and rotor position estimations with and without the PLL. In [11] and [29], the PLL was tuned such that the resonance frequency was 50 rad/s.

In this master thesis, resonance frequencies of 60, 70, and 80 rad/s were added for comparison. Simulations were also performed with $\omega_0 = 40$ and $\omega_0 = 100$, but these scenarios were omitted from the figure as they drastically reduced the performance. The graphs clearly show that a resonance frequency of 80 rad/s gives the most accurate estimations. The resonance frequencies of 60 and 70 rad/s also improve the estimations compared to not using the PLL.

Then, the stator resistance was accurately estimated, and a DC voltage offset of 2V was added to one of the stator voltages. In [11], it was stated that the PLL is especially effective if the estimated signal oscillates around the actual signal. This is the case for the rotor position when a DC offset is applied, evident from Figure 7.18. The PLL was tuned such that ω_0 was set to 50 and 80 rad/s, and the results were compared to the closed-loop observer without the PLL. Figure 7.21 shows the results of these simulations. From the error curves, it is evident that not using a PLL provides the most accurate stator flux linkage and rotor position estimations at low speeds. Increasing the resonance frequency from 50 to 80 rad/s does however improve the performance when using a PLL.

Figure 7.22 shows a zoomed-in view of the same graphs between 0.7 and 2.2 seconds, when the speed is higher. The graphs show that the stator flux linkage and rotor position estimates at higher speeds are more accurate when using a PLL with $\omega_0 = 80$ rad/s.

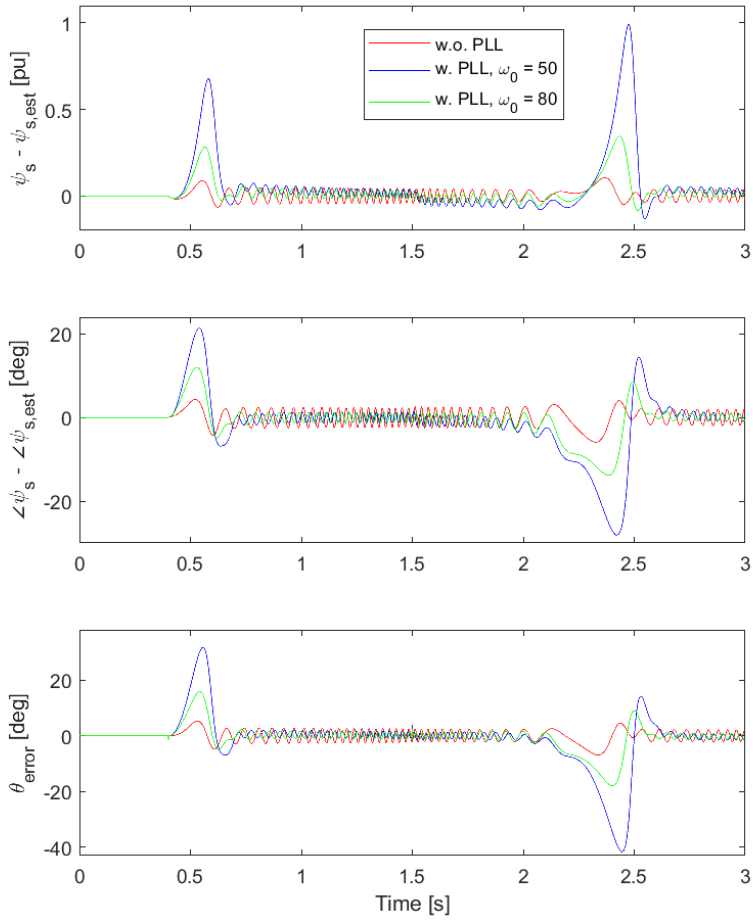

Figure 7.21: Estimation errors with and without PLL, 2V offset

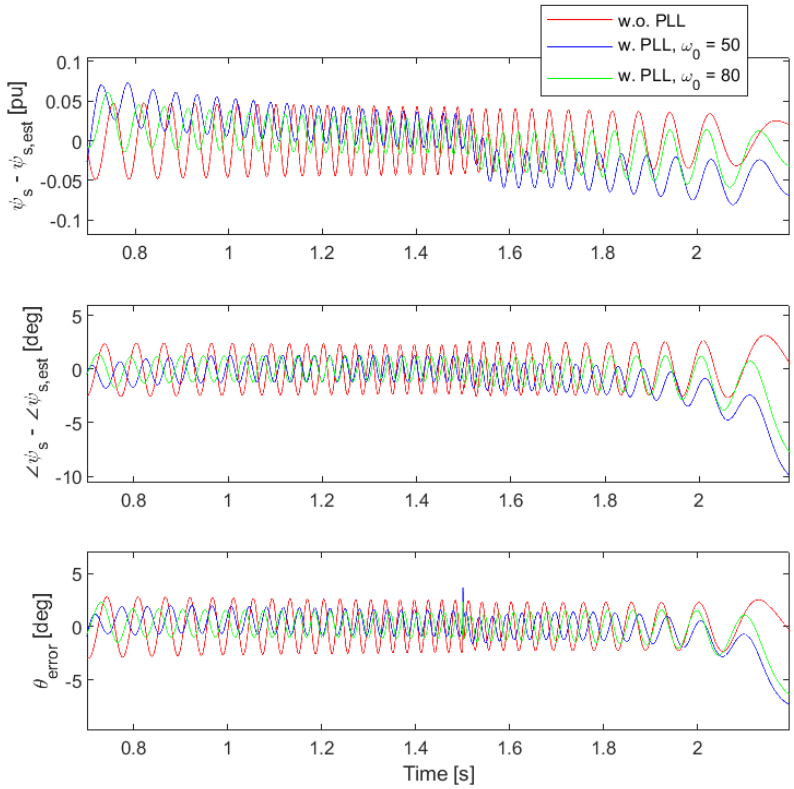

Figure 7.22: Estimation errors with and without PLL, 2V offset, 0.7-2.2 seconds

Chapter 8: Discussion

In this chapter, the simulation results from Chapter 7 are discussed and analyzed.

The field current controller was tuned by modulus optimum and was able to follow a varying field current reference accurately and fast. However, by doubling the gain calculated by modulus optimum, the accuracy was increased at the cost of a small overshoot. Doubling the gain increased the bandwidth, evident from Figure 7.3, although the phase margin was reduced slightly. By combining a twice as big proportional gain with an integral term divided by two, the field current reached its reference value faster, while having the same overshoot. This is evident from Figure 7.2.

In the specialization project [29], the PI controller in the feedback loop was tuned by developing a transfer function from ψ_{si} to the estimated stator flux linkage, comparing this to a general second-order transfer function in [39], and setting ω_0 to different percentages of the nominal speed. In this master thesis, this method was compared to tuning the PI controller by symmetrical optimum. Comparing Figure 7.9 to Figure 7.4 and 7.5, it is evident that tuning the controller by symmetrical optimum leads to less oscillatory errors when the stator resistance is underestimated. The peaks at start-up and when crossing zero speed are of approximately the same magnitude. However, the PI controller tuned by the 5 % scenario was able to dampen estimation errors due to a DC offset more efficiently, evident from comparing Figure 7.6 and 7.7 to Figure 7.10.

Sensorless control of a separately excited synchronous machine has been simulated in the MATLAB/Simulink environment. The sensitivity to errors in estimations

of the stator resistance, inductances in the d- and q-axis and damper winding resistances have all been analyzed in this report.

Figure 7.12 and 7.13 show that the stator flux linkage and rotor position are estimated with high accuracy when the stator resistance is underestimated and overestimated, respectively. The exceptions are the peaks at start-up and when the motor crosses zero-speed and starts rotating in the other direction. The performance during low-speed operation is a well-known problem of the voltage model, but from the figures, it is evident that also the combination method has room for improvement in this speed range. The overestimation of the stator resistance causes a slightly larger amplitude error than the underestimation, while the flux linkage angle error and rotor position error are slightly smaller.

In [9], it was stated that stator resistance compensations are not so important, as the current model should dominate in this speed region. In this thesis, however, the rotor position of the voltage model is used as input to the current model. Figure 7.12 and 7.13 show that the error curves of the stator flux linkage angle and rotor position angle are very similar, suggesting that the stator flux linkage errors at low speeds are caused by this rotor position error calculated by the voltage model. In the future, the same flux observer could be combined with a different way of calculating θ, in order to estimate the stator flux linkage more accurately in the low-speed region. It can also be observed from Figure 7.12 and 7.13 that the error peaks of the over- and underestimation are of the opposite sign. This can be explained using Equation 3.1, repeated here:

$$\psi_s = \int_0^t (u_s - r_s i_s) dt \tag{8.1}$$

When the resistance is underestimated, the estimated stator flux linkage will become larger than the actual value. Similarly, an overestimation of r_s causes the stator flux linkage estimate to become too small.

The equations of the current model, Equation 3.2-3.6, reveal that the current model depends on the accuracy of the inductances. This is also evident in the

simulation results of the scenarios where the inductances were under- and overestimated. Figure 7.14 shows that the combination method estimates the stator flux linkage quite effectively even when x_q is erroneously estimated. During startup, the stator flux linkage angle and amplitude are accurately estimated, and there are relatively small peaks when crossing zero speed. There are larger errors for the rotor position error, and this also has a small spike at the peak speed, when the motor transitions from increasing the speed to decreasing it. A reason for this can be because the q-axis inductance is used to estimate the rotor position, as can be seen from Equation 3.8.

Figure 7.15 reveals that when x_d is overestimated by 20%, the actual stator flux linkage starts increasing, suggesting that there is something wrong with the Simulink model. This theory was strengthened by the fact that the same thing happened when the machine was running with a position sensor. The source of this error has not been identified, and the same observation was made in [11]. In Figure 10.2 in Appendix D, the inductance was overestimated by 10 %, and the stator flux linkage behaves normally, keeping its value around 1 pu. This suggests that there is a certain limit of maximum d-axis inductance, after which the stator flux linkage increases out of control. In [35], it was argued that the inductances are easier to estimate than the resistances, as they only depend on saturation. Taking this into consideration, it could be that a deviation of 20 % from the actual value is unrealistically high, and that Figure 10.2 gives a better illustration of the sensitivity to the d-axis inductance.

When the d-axis inductance is underestimated by 20%, the stator flux linkage amplitude estimate is relatively accurate. The stator flux linkage angle and rotor position, on the other hand, deviate around 20° from the actual angles at low speeds. Compared to Figure 7.14, it is clear that the inductance in the d-axis has more influence on the stator flux linkage than the inductance in the q-axis. This is because the flux linkage in the d-axis, ψ_d, is much greater than the flux linkage of the q-axis, ψ_q. An error in the estimation of x_d will thus have a bigger impact on the stator flux linkage estimation than an error in x_q. Moreover, the value of x_d is twice as large as x_q.

Erroneously estimated damper winding resistances were simulated, with the results presented in Figure 7.16 and 7.17. The damper winding resistance in the q-axis is included in the current model equations, but changing r_Q does not influence the stator flux linkage estimation considerably. The graphs show minimal amplitude and angle errors, while the rotor position angle error shows a similar behavior as when the d-axis inductance was erroneously estimated. Like the d-axis inductance, the damper winding resistance is included in Equation 3.8. In the equation for the rotor position, T_Q is defined as:

$$T_Q = \frac{x_{Mq}}{\omega_n r_{Rq}}, \tag{8.2}$$

where r_{Rq} in turn is defined as:

$$r_{Rq} = \frac{r_Q}{(1+\sigma_Q)^2} \tag{8.3}$$

Unlike r_Q, the damper winding resistance in the direct axis, r_D, significantly reduces the accuracy of the stator flux linkage estimations. Both the underestimation and overestimation also lead to an oscillatory error, evident from Figure 7.17. A similar argumentation as for x_d can be made to explain this. r_D is included in the equations of the current model, like r_Q. However, as the flux linkage in the d-axis is greater than in the q-axis, errors in the estimation of r_D will have a more significant influence on the stator flux linkage estimations than an erroneously estimated r_Q.

When a DC offset of 2V was applied to one of the stator voltage phases, the PI controller tuned by symmetrical optimum did not provide the same dampening effect on the oscillatory error as for instance tuning after $\omega_0 = 0.05\omega_n$. The second graph in Figure 7.18 showing the real and estimated stator flux linkage reveals that the estimated stator flux linkage oscillates around the real one without getting dampened. The errors are slightly larger at startup and when crossing zero speed, for aforementioned reasons.

A longer simulation was performed with a slower crossing of the zero-speed. Figure 7.19 reveals that the stator flux linkage is still estimated accurately with the same low-speed exceptions, but the last error peak now lasts longer, approximately 1 second. The estimations are thus inaccurate in the speed interval [-0.05, 0.05] pu. As the nominal speed is 1500 rpm (obtained from Equation 2.1), the stator flux linkage and rotor position are accurately estimated above 75 rpm. For comparison, the active flux-based sensorless control in [9] provided high performance starting from 15 rpm. This goes to show that there is room for improvements in the model. As the stator flux linkage is calculated in the same way in [9] as in this thesis, improvements can possibly be made by changing the way θ is calculated and making it more accurate at low speeds.

In order to improve the estimations, a PLL was used to filter the rotor position input to the current model. In the specialization project [29], the PLL was able to dampen the magnitude of the oscillatory errors. However, the peaks at low speeds were larger than when the combination of the voltage and current model was used without the PLL. Figure 7.20 shows that by changing the resonance frequency to 80 rad/s, the errors can be reduced drastically when the stator resistance is underestimated. On the other hand, the estimations at low speeds were more accurate without a PLL when a DC offset was applied to the voltage measurements. At higher speeds, though, the PLL with $\omega_0 = 80$ rad/s was able to reduce the errors slightly.

Chapter 9: Conclusion

In this master thesis, sensorless control of a separately excited synchronous machine has been investigated. Flux models have been developed in order to run the machine without position or speed sensors, and a combination of the voltage model and the current model has been tested in Simulink.

The field current controller has been tuned according to modulus optimum. In addition, the PI controller in the feedback loop of the combination of the voltage model and the current model has been tuned by symmetrical optimum in order to improve the performance during sensorless control. The sensitivity to erroneously estimated or measured parameters in the model has been tested thoroughly in Simulink. Moreover, a PLL has been used to filter the rotor position that is input to the current model, in an attempt to improve the accuracy of the estimations further.

The field current controller and the PI controller have been tuned according to modulus optimum and symmetrical optimum, respectively. The testing of the field current controller revealed that the existing controller with parameters calculated in [10] provided a field current that followed its reference accurately. However, by dividing the integral term calculated by modulus optimum by two, the field current followed its reference more rapidly. The PI controller in the closed-loop observer was tuned by symmetrical optimum in this master thesis, and the performance was compared to an experimental tuning method presented in [29]. By tuning the controller in this way, the stator flux linkage was estimated more accurately when the stator resistance was underestimated. However, when correcting for drifting due to a DC offset in the voltage measurements, the tuning method where ω_0 was set to 5% of the nominal electric speed provided the most accurate stator flux

linkage and rotor position estimates.

The closed-loop observer combining the voltage and current model estimated the stator flux linkage accurately, except during startup and when crossing zero speed. An erroneously estimated stator resistance led to low-speed errors as large as 0.2 pu for the stator flux linkage amplitude and 20° for the angle. These errors did not change magnitude when the zero-crossing was slower, but the peak errors lasted for a longer duration.

An underestimated d-axis inductance caused large errors in the estimations of the stator flux linkage and rotor position. The stator flux linkage amplitude and angle were more accurately estimated when the q-axis inductance deviated from the actual value, but this also led to significant errors in the rotor position angle. This is because the implicit equation for the rotor position is dependent on the d-axis inductance. For this reason, inaccurately estimated damper winding resistances also led to inaccurate rotor position estimates. The current model was sensitive to the damper winding resistance in the d-axis, while the damper winding resistance in the quadrature axis had little impact on the estimation of the stator flux linkage. The most prominent stator flux linkage error occurred when a DC offset was applied to one of the stator voltage phases. This made the estimated stator flux linkage oscillate around the real value with a relatively large amplitude.

A PLL block was used to filter the rotor position estimated from the voltage model. To be able to improve the performance, the PLL had to be tuned. By changing the resonance frequency from 50 to 80 rad/s, the accuracy of the estimations of the stator flux linkage and rotor position were greatly improved when the stator resistance was underestimated. When a DC offset was applied to the voltage measurements, the estimations were slightly improved by the PLL, except at low speeds where the estimates were more accurate without the PLL. Tuning the PLL such that $\omega_0 = 80$ rad/s did however improve the estimations compared to 50 rad/s that was used previously.

Chapter 10: Further work

In the future, tests of the sensorless performance of a synchronous machine should be performed in the laboratory on an actual machine. A new control platform is currently being developed at NTNU, where a picoZed board and a board developed at SINTEF can be used for the implementation of the control structures. Xilinx SDK can be used as the software environment for programming the board, using the C++ programming language. To program the FPGA, Vivado can be used, in combination with the System Generator for DSP add-on in Simulink. The System Generator enables Simulink to be used for FPGA-programming in an easier block structure, without having to code VHDL. A PESC software group consisting of the supervisor of the author, Roy Nilsen, Ph.D. students and master students (including the author) has been formed this spring, with the goal of having a common platform for software development at the Department of Electric Power Engineering. Unfortunately, not enough to time was available to be able to test this control system in the laboratory, but this is something that can be done in the future. Performing tests in the laboratory can, in addition to being more realistic, save a lot of time compared to the time-consuming simulations in Simulink.

In the parameter sensitivity section in this master thesis, the parameters were erroneously estimated for the entire simulation. How sudden changes to the parameters affect the control system can be tested in the future. Online and offline parameter estimation techniques can be implemented in order to minimize the large estimation errors that were tested in this thesis. When the d-axis inductance was overestimated by 20%, the actual stator flux linkage started increasing towards 10 pu. This suggests that there might be something wrong with the Simulink model, and should be investigated further in the future.

To be able to compare the effects of the different parameters, the same torque reference was applied to all the simulations in Section 7.2.1. In [11], the acceleration was adjusted by changing the moment of inertia, using the same applied torque reference. As the voltage model's sensitivity to the stator resistance increases with the torque reference at low speeds [11], more investigation can be done on the performance of the combination method with a varying torque. Performing dynamic analysis in the field weakening region of the machine has also been suggested in [11], as the current model is sensitive to field weakening.

The PLL was able to improve the performance significantly when the stator resistance was underestimated. However, when using a PLL, the estimation errors became larger at low speeds when a DC voltage offset was applied. Further tuning and improvements of the PLL can be done in order to reduce, or ideally remove, this disadvantage.

Bibliography

[1] A. E. Fitzgerald, Charles Kingsley Jr., S. D. U., 2003. Electric Machinery, Sixth Edition. McGraw-Hill.

[2] Acarnley, P. P., Watson, J. F., April 2006. Review of position-sensorless operation of brushless permanent-magnet machines. IEEE Transactions on Industrial Electronics 53 (2), 352–362.

[3] Adib, R., Murdock, H., Appavou, F., Brown, A., Epp, B., Leidreiter, A., Lins, C., Murdock, H., Musolino, E., Petrichenko, K., et al., 2015. Renewables 2015 global status report. Paris: REN21 Secretariat.

[4] Araya, N. B., 2012. Modelling and Control of Six-Phase Induction Motor Drive, Master thesis. NTNU.

[5] Bertoluzzo, M., Buja, G., Menis, R., Sep. 2007. A direct torque control scheme for induction motor drives using the current model flux estimation. In: 2007 IEEE International Symposium on Diagnostics for Electric Machines, Power Electronics and Drives. pp. 185–190.

[6] Bjørkhaug, E. H., 2017. Adjustable Speed of Synchronous Machine for Hydro Power Application, Master thesis. NTNU.

[7] Blaschke, F., 1972. The principle of field orientation as applied to the new transvector closed loop control system for rotating field machines. Siemens review 34, 217–220.

[8] Boldea, I., 2002. Direct Torque and Flux Control (DTFC) of AC Drives, Chapter 9. Elsevier Science & Technology.

[9] Boldea, I., Andreescu, G. D., Rossi, C., Pilati, A., Casadei, D., Sep. 2009. Active flux based motion-sensorless vector control of dc-excited synchronous machines. In: 2009 IEEE Energy Conversion Congress and Exposition. pp. 2496–2503.

[10] Bolstad, M., 2017. Control of Synchronous Machines Used in ASH, Specialization Project. NTNU.

[11] Bolstad, M., 2018. Sensorless Control of Synchronous Machines used in Adjustable Speed Hydro, Master thesis. NTNU.

[12] Bühler, H., 1977. Einführung in die Theorie Geregelter Drehstromantriebe, Band 1. Birkhäuser Verlag Basel Und Stuttgart.

[13] Bühler, H., 1977. Einführung in die Theorie Geregelter Drehstromantriebe, Band 2. Birkhäuser Verlag Basel Und Stuttgart.

[14] Depenbrock, M., June 1987. Direct self-control (dsc) of inverter fed induction machine. In: 1987 IEEE Power Electronics Specialists Conference. pp. 632–641.

[15] Dirk Paulus, Jean-François Stumper, R. K., 2012. Sensorless Control of Synchronous Machines Based on Direct Speed and Position Estimation in Polar Stator-Current Coordinates. IEEE.

[16] Duesterhoeft, W. C., Schulz, M. W., Clarke, E., July 1951. Determination of instantaneous currents and voltages by means of alpha, beta, and zero components. Transactions of the American Institute of Electrical Engineers 70 (2), 1248–1255.

[17] Fossen, B., 2016. Modelling and Identification of Multi-Phase Machines. NTNU.

[18] Frede Blaabjerg, K. M., 2017. Wind Energy Systems. IEEE.

[19] Grøvan, O., 2004. Identifikasjon og regulering av en synkronmotordrift, Master thesis. NTNU.

[20] Hanselman, D., 2006. Permanent Magnet Motor Design. Magna Physics Publ.

[21] Hansen, S., Malinowski, M., Blaabjerg, F., Kazmierkowski, M. P., Feb 2000. Sensorless control strategies for pwm rectifier. In: APEC 2000. Fifteenth Annual IEEE Applied Power Electronics Conference and Exposition (Cat. No.00CH37058). Vol. 2. pp. 832–838 vol.2.

[22] Haugen, F., 1994. Regulering av dynamiske systemer. Tapir forlag.

[23] Haugen, F., 2010. Discretization of simulator, filter, and pid controller. Tech. Teach, http://www. mic-journal. no/PDF/ref/Haugen2010. pdf.

[24] Jain, A. K., Ranganathan, V. T., March 2011. Modeling and field oriented control of salient pole wound field synchronous machine in stator flux coordinates. IEEE Transactions on Industrial Electronics 58 (3), 960–970.

[25] Kothari, D. P., Nagrath, I. J., 2010. Electric Machines, Fourth Edition. McGraw Hill Education.

[26] Lipo, T., 2012. Analysis of Synchronous Machines, Second Edition. Taylor & Francis.

[27] M. C. Paicu, I. Boldea, G.-D. A. F. B., 2009. Very low speed performance of active flux based sensorless control: interior permanent magnet synchronous motor vector control versus direct torque and flux control. IET Electric Power Applications, Vol 3, Iss. 6, pp. 551-561.

[28] Matsui, N., Shigyo, M., Jan 1992. Brushless dc motor control without position and speed sensors. IEEE Transactions on Industry Applications 28 (1), 120–127.

[29] Mjell, H. L., 2018. Sensorless Control of Synchronous Machines used in ASH, Specialization project. NTNU.

[30] Mørkved, E., 2017. Sensorless Control of a 6-phase Induction Machine, Master thesis. NTNU.

[31] Nestli, T. F., 1995. Modelling and identification of induction machines. NTH.

[32] Niemelä, M., 1999. Position sensorless electrically excited synchronous motor drive for industrial use based on direct flux linkage and torque control. Lappeenranta University of Technology.

[33] Niemelä, M., Luukko, J., Pyrhönen, O., Kaukonen, J., 2000. Position-sensorless direct-torque-controlled synchronous motor drive for ship propulsion. European Transactions on Electrical Power 10 (6), 353–360.

[34] Nilsen, R., 2004. Elektriske motordrifter, Kap. 6: Synkronmotordrifter. NTNU.

[35] Nilsen, R., Spring 2018. TET4120 Electric Drives. NTNU.

[36] Park, R. H., 1929. Two-reaction theory of synchronous machines generalized method of analysis-part I. IEEE.

[37] Pyrhönen, O., 1998. Analysis and Control of Excitation, Field Weakening and Stability in Direct Torque Controlled Electrically Excited Synchronous Motor Drives. Lappeenranta University of Technology.

[38] Roy Nilsen, T. N., 1994. Evaluation And Comparison of Predictor Models For Rotor Flux Calculation In Induction Motors. IEEE.

[39] Trond Andresen, Jens G. Balchen, B. A. F., 2016. Reguleringsteknikk. Institutt for teknisk kybernetikk, NTNU.

[40] Urmas Raudsaar, Imre Drovtar, A. R., 2014. Overview - Pumped-Hydro Energy Storage for Balancing Wind Energy Forecast Errors. IEEE.

Appendix

A Estimation of rotor position and speed

In this section, the full derivation of Equation 3.8 from [10, 11] is summarized. The same summary can be found in the specialization project [] From Figure 3.1, repeated here for convenience, it can be seen that:

$$i_q = i_s cos(90^\circ - \varphi_s^s + \theta) = i_s sin(\varphi_s^s - \theta) \tag{A.1}$$

$$sin(\varepsilon_s^r) = \frac{\psi_q}{\psi_s} = \frac{\sigma_{qQ} x_q i_q + \psi_{Rq}}{\psi_s} \tag{A.2}$$

By using the expression for ψ_{Rq} in Equation 2.85, this becomes:

$$sin(\varepsilon_s^r) = \frac{\sigma_{qQ} x_q i_q + \frac{x_{Mq}}{1+T_Q s} i_q}{\psi_s} = \frac{\sigma_{qQ} x_q + \frac{x_{Mq}}{1+T_Q s}}{\psi_s} i_q \tag{A.3}$$

Then the expression for i_q in Equation A.1 can be inserted into the equation, and Equation A.4 is obtained.

$$sin(\varepsilon_s^r) = \frac{\sigma_{qQ} x_q + \frac{x_{Mq}}{1+T_Q s}}{\psi_s} i_s sin(\varphi_s^s - \theta) \tag{A.4}$$

From the figure, there is a relationship between ε_s^r, ε_s^s and θ, shown in Equation A.5.

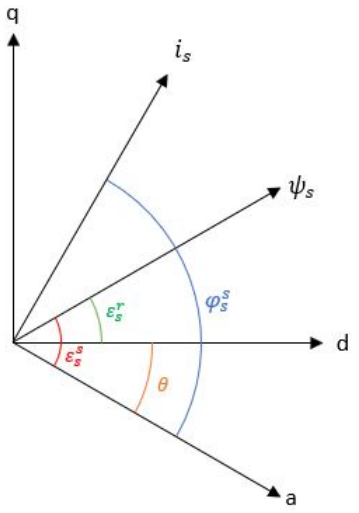

Figure 10.1: Space vector diagram showing the relationship between different angles

$$\varepsilon_s^r = \varepsilon_s^s - \theta \tag{A.5}$$

Then, the final implicit equation (Equation 3.8) is obtained by inserting A.5 into A.4:

$$sin(\varepsilon_s^s - \theta) = \frac{\sigma_{qQ} x_q + \frac{x_{Mq}}{1+T_Q s}}{\psi_s} i_s sin(\varphi_s^s - \theta) \tag{A.6}$$

It can then be discretized by using the trapezoidal approximation [39, p. 511].

B Machine parameters

The parameters of the synchronous machine used in the Simulink model are shown in Table 10.1.

Parameter	**Symbol**	**Value**
Nominal line-line voltage [V_{rms}]	U_n	400
Nominal current [A_{rms}]	I_n	21
Nominal frequency [Hz]	f_n	50
Field winding base current [A]	$I_{f,base}$	4.7576
Number of pole pairs	p	2
Stator resistance [pu]	r_s	0.048
d-axis damper resistance [pu]	r_D	0.02
q-axis damper resistance [pu]	r_Q	0.03
Field winding resistance [pu]	r_f	0.02
d-axis stator reactance [pu]	x_d	1.17
q-axis stator reactance [pu]	x_q	0.57
Field winding reactance [pu]	x_f	1.32
d-axis damper reactance [pu]	x_D	1.12
q-axis damper reactance [pu]	x_Q	0.59
leakage stator reactance [pu]	x_σ	0.12

Table 10.1: Parameters of the synchronous machine

C Constants in the per unit equations

In this section, the constants used in the per unit equations (Equation 2.81 to 2.88) are defined. The full derivation of the per unit equations can be found in [10, 11].

$$\sigma_{dD} = 1 - \frac{1}{(1+\sigma_d)(1+\sigma_D)} \tag{C.1}$$

$$\sigma_{Df} = 1 - \frac{1}{(1+\sigma_f)(1+\sigma_D)} \tag{C.2}$$

$$\sigma_{qQ} = 1 - \frac{1}{(1+\sigma_q)(1+\sigma_Q)} \tag{C.3}$$

$$r_d^{`} = r_s + \frac{r_D}{(1+\sigma_D)^2} \tag{C.4}$$

$$r_q^{`} = r_s + \frac{r_Q}{(1+\sigma_Q)^2} \tag{C.5}$$

$$r_f^{`} = r_f + \frac{r_D}{(1+\sigma_D)^2} \tag{C.6}$$

$$r_d^{``} = r_s + (1-k_{fD})\frac{r_D}{(1+\sigma_D)^2} \tag{C.7}$$

$$r_f^{``} = r_f + (1-k_{dD})\frac{r_D}{(1+\sigma_D)^2} \tag{C.8}$$

$$k_{fD} = \frac{\sigma_D}{\sigma_f(1+\sigma_D+\frac{\sigma_D}{\sigma_f})} \tag{C.9}$$

$$k_{dD} = \frac{\sigma_D}{\sigma_d(1+\sigma_D+\frac{\sigma_D}{\sigma_d})} \tag{C.10}$$

$$\sigma_d^{``} = \sigma_{dD} - k_{fD}\frac{\sigma_D}{(1+\sigma_d)(1+\sigma_D)} \tag{C.11}$$

$$\sigma_f^{``} = \sigma_{Df} - k_{dD}\frac{\sigma_D}{(1+\sigma_f)(1+\sigma_D)} \tag{C.12}$$

(C.13)

$$r_{Rd} = \frac{r_D}{(1+\sigma_D)^2} \tag{C.14}$$

$$r_{Rq} = \frac{r_Q}{(1+\sigma_Q)^2} \tag{C.15}$$

$$\psi_{Rd} = \frac{\psi_D}{1+\sigma_D} \tag{C.16}$$

$$\psi_{Rq} = \frac{\psi_Q}{1+\sigma_Q} \tag{C.17}$$

$$x_{Md} = \frac{x_{md}}{1 + \sigma_D} \tag{C.18}$$

$$x_{Mq} = \frac{x_{mq}}{1 + \sigma_Q} \tag{C.19}$$

The time constants T_D and T_Q can be defined as:

$$T_D = \frac{x_{Md}}{\omega_n r_{Rd}} \tag{C.20}$$

$$T_Q = \frac{x_{Mq}}{\omega_n r_{Rq}} \tag{C.21}$$

The final per unit equations, using these constants, are presented in Equation 2.81 to 2.88.

D x_d overestimated by 10 %

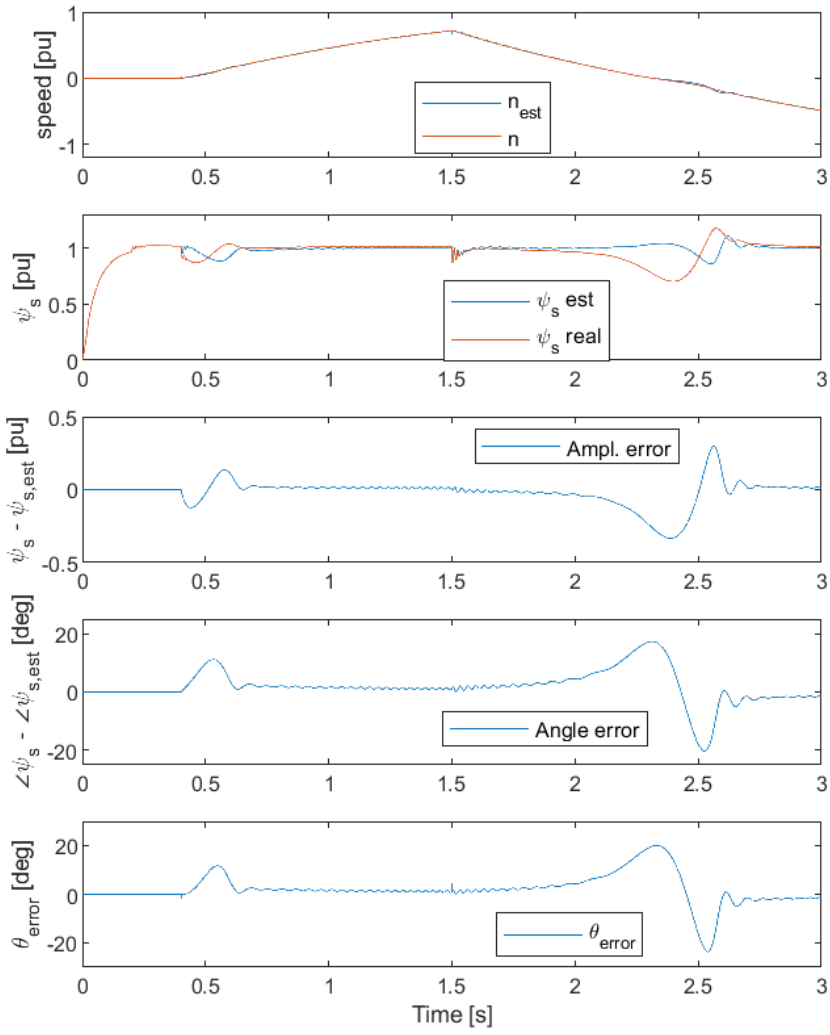

Figure 10.2: Overestimated d-axis inductance, $\hat{x}_d = 1.1x_d$

E Simulink

The outer layer of the Simulink model is repeated below. The outer layer of the control system block in Simulink is shown in Figure 10.4. Figure 10.5 shows the voltage model, the current model, and how they are combined with a PI controller in the feedback loop.

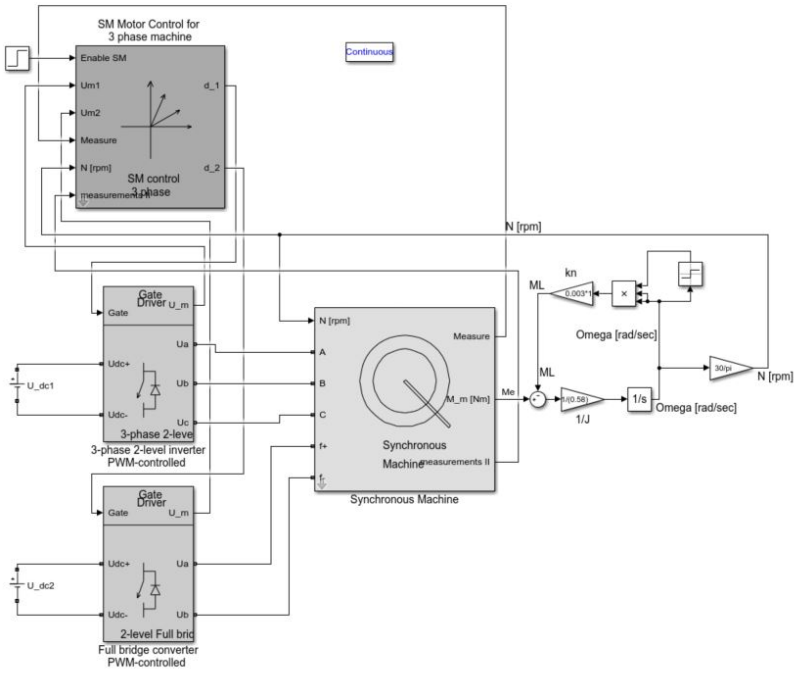

Figure 10.3: Outer layer of the Simulink model

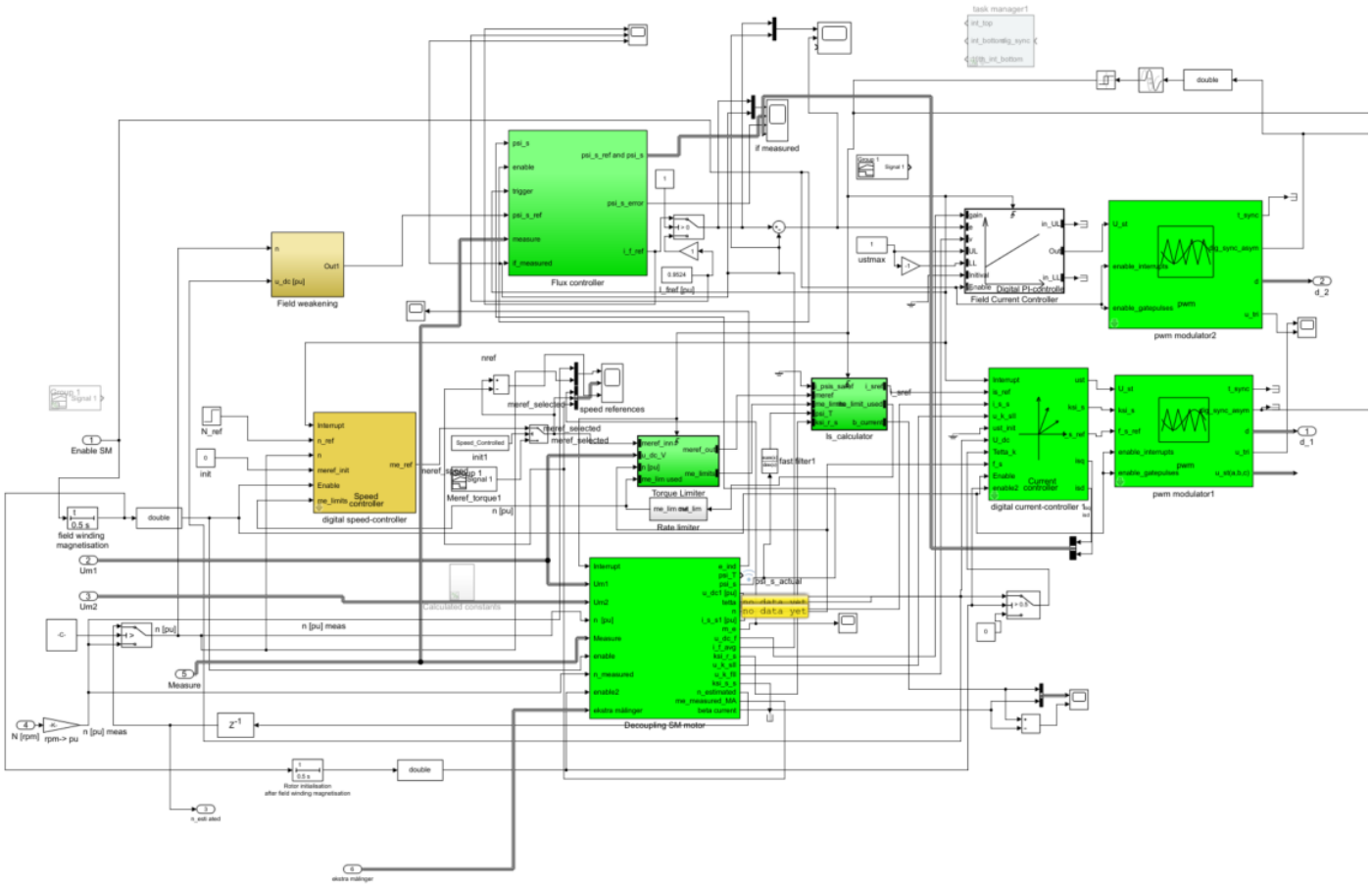

Figure 10.4: Outer layer of the control block

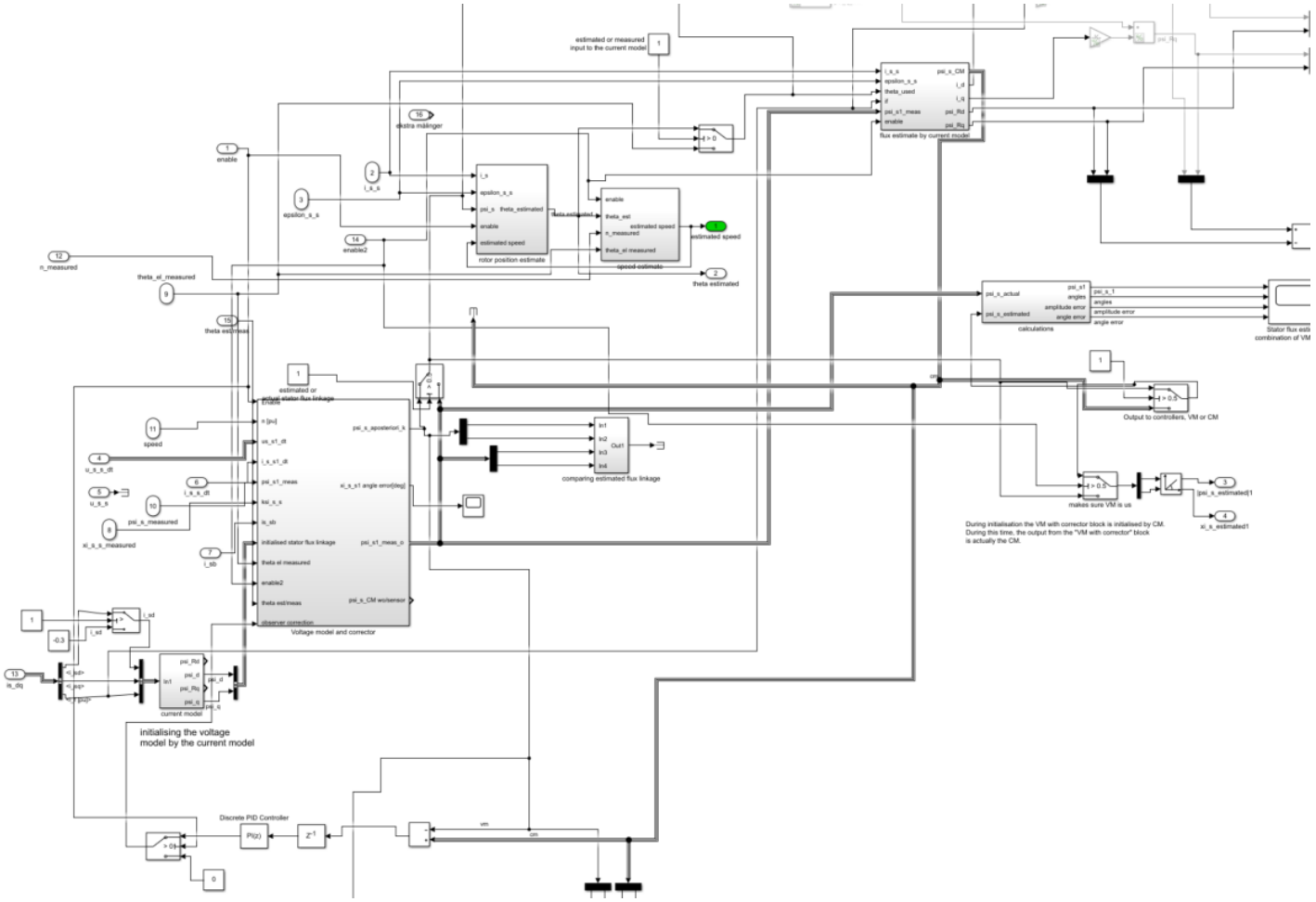

Figure 10.5: The Simulink structure showing the voltage model, the current model and the PI controller

Håkon Laaveg Mjell

Sensorless Control of Synchronous Machines used in ASH

NTNU
Kunnskap for en bedre verden